

1  
2  
3  
4  
5  
6  
7  
8  
9  
10  
11  
12  
13  
14  
15  
16  
17  
18  
19  
20  
21  
22  
23  
24  
25  
26  
27  
28  
29  
30  
31  
32  
33  
34  
35  
36  
37  
38  
39  
40

## An approximate line attractor in the hypothalamus that encodes an aggressive internal state

Aditya Nair<sup>1,2,3,4</sup>, Tomomi Karigo<sup>2,3,4</sup>, Bin Yang<sup>2,3,4</sup>, Scott W Linderman<sup>5,6</sup>,  
David J Anderson<sup>2,3,4\*</sup> & Ann Kennedy<sup>7\*</sup>

<sup>1</sup>Computation and Neural Systems, Caltech, Pasadena, CA, USA

<sup>2</sup>Division of Biology and Biological Engineering, Caltech, Pasadena, CA, USA

<sup>3</sup>Howard Hughes Medical Institute, Caltech, Pasadena, CA, USA

<sup>4</sup>Tianqiao and Chrissy Chen Institute for Neuroscience  
Caltech, Pasadena, CA 91125, USA

<sup>5</sup>Department of Statistics, Stanford University, Stanford, CA, USA

<sup>6</sup>Wu Tsai Neurosciences Institute, Stanford University, Stanford, CA, USA

<sup>7</sup>Department of Neuroscience, Feinberg School of Medicine Northwestern University,  
Chicago, IL 60611, USA

\*Corresponding authors: D.J.A, [wuwei@caltech.edu](mailto:wuwei@caltech.edu);  
A.K, [ann.kennedy@northwestern.edu](mailto:ann.kennedy@northwestern.edu)

## 41 Summary

42 The hypothalamus plays a key role in regulating innate behaviors. It is widely believed to  
43 function as a system of ‘labeled lines’, containing behavior-specific neurons with  
44 characteristic transcriptomic and connectomic profiles. This view however fails to explain  
45 why, although activation of estrogen receptor-1 (Esr1) expressing neurons in the  
46 ventromedial hypothalamus (VMHvl) promotes aggression, few VMHvl neurons are tuned  
47 to attack. To address this paradox, we adopted an unsupervised dynamical systems  
48 framework to analyze population activity among VMHvl<sup>Esr1</sup> neurons during aggression.  
49 We discovered that this activity contains an “integration” dimension exhibiting slow-  
50 ramping dynamics and persistent activity that correlates with escalating aggressiveness.  
51 These dynamics are implemented as an approximate line attractor in state space. Our  
52 analysis suggests a function for VMHvl to encode the intensity of behavior-relevant motive  
53 states using line attractors. This view reconciles observational and perturbational studies  
54 of VMHvl, and reveals a new mode of neural computation in the hypothalamus.

## 55 Introduction

56 Innate behaviors are typically triggered by specific exteroceptive or interoceptive  
57 sensory cues that initiate a cascade of activity in the brain (Tinbergen, 1951). Cue-evoked  
58 neural activity in primary sensory or interoceptive brain regions modifies activity in  
59 downstream areas. This integration of new signals into the brain's ongoing dynamics can  
60 drive a behavioral reaction and/or generate an internal motive state such as arousal or  
61 fear that may modify expression of future behavior. Where and how internal states are  
62 generated, and how internal states and sensory cues are jointly transformed into behavior  
63 by the brain, remains an important unsolved problem.

64 The hypothalamus has been implicated in the expression of innate behaviors for  
65 well over a century (Saper and Lowell, 2014). These include homeostatic behaviors such  
66 as feeding or drinking, as well as predator defense, grooming, mating, and aggression  
67 (Canteras, 2002; Hess, 1927; Hess and Brügger, 1943; Leibowitz, 1992). More recent  
68 studies have used genetically targeted optogenetic or chemogenetic perturbations to  
69 demonstrate that specific hypothalamic subpopulations control particular behaviors in a  
70 dominant manner (Anderson, 2016; Augustine et al., 2020; Chen and Hong, 2018;  
71 Hashikawa et al., 2017b; Sternson, 2013) (We use the term “dominant” to describe the  
72 effect of experimentally activating a neural population on a particular behavior, and to  
73 distinguish this population from neurons within the same brain region that may “encode”  
74 or “represent” other behavior(s) in their firing rates but which are not affected by such  
75 perturbations; see Karigo et al., 2021.) In male mice, for example, estrogen receptor type  
76 1 (Esr1) and progesterone receptor (PR)-expressing glutamatergic neurons in the  
77 ventrolateral subdivision of ventromedial hypothalamus (VMHvl) play a dominant role in  
78 the control of aggression in male mice (Lee et al., 2014; Yang et al., 2017; Zha and Xu,  
79 2021). Conversely, Esr1<sup>+</sup> GABAergic neurons in the medial preoptic area (MPOA) play a  
80 dominant role in mating behaviors (Chen et al., 2021; Gao et al., 2019; Karigo et al., 2021;  
81 Tschida et al., 2019; Wei et al., 2018).

82 An important question is how the dominant behavioral influences of a given neural  
83 subclass, as identified in artificial activation experiments, relate to its population dynamics  
84 or coding properties during spontaneous occurrences of those same behaviors (Jazayeri

85 [and Afraz, 2017](#)). In the case of MPOA, the dominant role of  $Esr1^+$ , VGAT<sup>+</sup> neurons in  
86 mating is in alignment with two other lines of investigation. First, calcium imaging  
87 experiments reveal neuronal subpopulations in the MPOA that are active during specific  
88 mating actions such as mounting or intromission ([Karigo et al., 2021](#)). And second, single  
89 cell RNA sequencing (scRNAseq) experiments have identified transcriptomically distinct  
90 MPOA neuronal subpopulations that express c-fos during specific reproductive social  
91 behaviors such as mating ([Moffitt et al., 2018](#)) ([Figure 1A](#)). Thus, in the case of MPOA,  
92 both observational and perturbational studies align to support a key role for  $Esr1^+$   
93 GABAergic neurons in the control of specific mating-related actions.

94 In contrast, while manipulations of VMHvl<sup>Esr1/PR</sup> neurons have revealed a dominant  
95 role for these neurons in aggression, there is only a weak correspondence between  
96 VMHvl<sup>Esr1</sup> neuron activity and specific occurrences of aggressive behavior; instead, most  
97 individual VMHvl<sup>Esr1</sup> neurons exhibit strong selectivity for either male or female  
98 conspecifics ([Remedios et al., 2017](#)). Although some neurons show weak selective  
99 modulation during aggression, mating, or investigative behavior, most cells exhibit mixed  
100 selectivity for multiple behaviors ([Karigo et al., 2021](#); [Remedios et al., 2017](#)). Furthermore,  
101 although VMHvl<sup>Esr1</sup> neurons exert a dominant influence on aggression, they are also  
102 required (albeit not sufficient) for normal levels of mating ([Karigo et al., 2021](#); [Yang et al.,](#)  
103 [2013](#)). These data suggest that the function of the male- vs. female-selective VMHvl<sup>Esr1</sup>  
104 neurons, as revealed by observational experiments, may be to encode conspecific sex  
105 identity ([Yang and Shah, 2014](#)), or an internal motive state that is strongly correlated with  
106 conspecific sex, i.e., aggressiveness ([Falkner et al., 2014](#); [Falkner et al., 2016](#)) vs. mating  
107 drive ([Zhang et al., 2021](#)). Because male mice typically exhibit aggression towards males  
108 and mating towards females, intruder sex and behavior are highly correlated, making it  
109 difficult to distinguish these alternatives. (However a subset of VMHvl<sup>Esr1</sup> neurons in  
110 female mice has been shown to promote aggression towards both males and females;  
111 ([Hashikawa et al., 2017a](#); [Liu et al., 2022](#))).

112 The failure to identify a robust encoding of aggressive behavior at the level of single  
113 neurons in VMHvl seems paradoxical given the high specificity of optogenetic and  
114 chemogenetic activation for aggressive behaviors, including dominance mounting and

115 attack ([Karigo et al., 2021](#); [Lee et al., 2014](#); [Yang et al., 2017](#)). It is especially puzzling in  
116 light of the strong correspondence between optogenetic phenotypes and behavior-  
117 specific single-cell tuning observed in MPOA (([Karigo et al., 2021](#); [Kohl et al., 2018](#); [Moffitt](#)  
118 [et al., 2018](#); [Wu et al., 2014](#)) This paradox has led us to investigate whether population-  
119 based, rather than single-neuron, coding might underlie the control of aggression by  
120 VMHvI<sup>Esr1</sup> neurons.

121 Here we use recurrent switching linear dynamical systems (rSLDS) ([Linderman et](#)  
122 [al., 2017](#)) analysis to investigate whether the dynamics of VMHvI<sup>Esr1</sup> population activity  
123 can reveal an encoding of aggressive behavior and/or drive in this nucleus. This analysis  
124 uncovered an approximate line attractor in neural activity space, progression along which  
125 is correlated with the intensity and type of aggressive behavior displayed. By contrast, in  
126 MPOA we observe rotational rather than line attractor dynamics, consistent with our  
127 observation of the sequential activation of behaviorally tuned MPOA neurons during  
128 mating. Taken together, our results reveal that different hypothalamic nuclei use different  
129 neural coding schemes to control closely related social behaviors. They also provide  
130 evidence for line attractors as a mechanism by which subcortical circuits may generate  
131 persistent and scalable internal states that shape the expression of survival behaviors.

## 132 Results

### 133 Cellular tuning analysis reveals behaviorally selective neural populations in MPOA 134 but not in VMHvl

135 Although optogenetic stimulation of VMHvl<sup>Esr1</sup> glutamatergic or MPOA<sup>Esr1</sup> GABAergic  
136 neurons evokes aggression and mating, respectively (Hashikawa et al., 2017a; Karigo et  
137 al., 2021; Lee et al., 2014; Wei et al., 2018; Yang et al., 2013), calcium imaging during  
138 social interaction reveals more complex patterns of neuronal activation (Figure 1A, B)  
139 (Karigo et al., 2021; Remedios et al., 2017). To illustrate these differences more clearly,  
140 we compared behavioral tuning at the level of individual Esr1<sup>+</sup> neurons in VMHvl vs.  
141 MPOA during dyadic social interaction. Specifically, we re-analyzed calcium imaging data  
142 (Karigo et al., 2021) recorded from Esr1<sup>+</sup> neurons in these nuclei using a head-mounted  
143 microendoscope (Ghosh et al., 2011; Ziv et al., 2013), in sexually experienced male  
144 C57Bl/6N<sup>Esr1-2A-Cre</sup> mice during standard resident-intruder assays, using male or female  
145 BalbC intruders (Figure 1C, D).

146 To compare the responses of Esr1<sup>+</sup> neurons in VMHvl and MPOA, we computed  
147 the mean activation of each imaged neuron during 14 different, manually annotated  
148 behavioral actions and grouped neurons by their normalized pattern of activation across  
149 all actions (VMHvl: N= 306 neurons from 3 mice; MPOA: N= 391 neurons from 4 mice.)  
150 This analysis revealed that many MPOA clusters contained neurons only active during  
151 specific social behaviors, such as intromission, ultrasonic vocalization-accompanied  
152 (USV<sup>+</sup>; reproductive) mounting, attack, and USV<sup>-</sup> (dominance) mounting (Figure 1E). A  
153 relatively small proportion was activated in a sex-specific but not behaviorally specific  
154 manner. In contrast, most neurons in VMHvl were broadly activated in an intruder sex-  
155 specific manner, with very few neurons showing preferential activation during specific  
156 behavioral actions (Karigo et al., 2021; Remedios et al., 2017) (Figure 1F). Most strikingly,  
157 we observed a higher proportion of attack-specific neurons in MPOA than in VMHvl,  
158 despite the former's dominant influence on mating.

159 This analysis indicates that MPOA and VMHvl cannot simply be considered  
160 analogous nuclei that govern opponent social behaviors in comparable fashion. MPOA

161 contains multiple distinct behaviorally-tuned subpopulations, consistent with c-fos -  
162 analysis that shows that this nucleus contains specific transcriptomic cell-types activated  
163 during different social behaviors (Kohl et al., 2018; Moffitt et al., 2018). In contrast, VMHvl  
164 contains very few neurons tuned to specific behaviors, consistent with the paucity of c-  
165 fos-labeled action-specific transcriptomic cell types in VMHvl (Kim et al., 2019). This is  
166 also consistent with the conclusions from our earlier imaging studies of VMHvl<sup>Esr1</sup> neurons,  
167 which examined a different dataset using choice probability analysis (Remedios et al.,  
168 2017).

### 169 **Unsupervised dynamical systems analysis of neural activity during social behavior**

170 Our analysis of single cell tuning among VMHvl<sup>Esr1</sup> neurons presented a paradox:  
171 optogenetic stimulation of these cells elicits specific social behaviors (aggressive sniffing,  
172 USV-mounting and attack (Karigo et al., 2021; Lee et al., 2014)), yet we observed only a  
173 few cells (<10%) that are selectively active during these specific behaviors ((Karigo et al.,  
174 2021; Remedios et al., 2017) and this study). However, the lack of neurons exclusively  
175 activated during a particular behavioral action such as attack does not mean that VMHvl  
176 contains no information about ongoing behavior. Indeed, we previously demonstrated that  
177 the occurrence of social behavior actions, including attack and investigation, could be  
178 decoded from the activity of VMHvl neurons (Remedios et al., 2017). Nevertheless, that  
179 analysis did not provide insight into how VMHvl population dynamics control behaviors or  
180 shape the transitions between them.

181 In other neural systems, population analysis via fit dynamical systems has helped  
182 identify the neural encoding of values that are not apparent in neuron-by-neuron analysis  
183 (Hulse and Jayaraman, 2020; Shenoy et al., 2013; Vyas et al., 2020). We therefore  
184 investigated whether behavioral representations among VMHvl<sup>Esr1</sup> neurons might be  
185 encoded at a population level, using an unsupervised dynamical systems approach.

186 To do so, we fit a dynamical model to the population activity of VMHvl<sup>Esr1</sup> cells from  
187 each of several (n=6) individual mice over the course of an entire male-male or male-  
188 female encounter (duration  $5.1 \pm 0.68$  minutes for male-male encounters and  $11.4 \pm 0.68$   
189 minutes for male-female encounters) Specifically, we fit a recurrent switching linear  
190 dynamical system (rSLDS) (Linderman et al., 2017), a class of model that approximates

191 a complex non-linear dynamical system using a composite of linear dynamical systems.  
192 The rSLDS model offers three features that make it useful for further analysis. First, by  
193 “switching” between linear systems, the model can approximate the dynamics of a  
194 complex nonlinear system, while still permitting the fit model to be analyzed using the  
195 abundance of techniques available for linear systems (Linderman et al., 2019). Second,  
196 rSLDS can model the contributions of both external input and intrinsic dynamics to the  
197 evolution of neural population activity. The intrinsic component of the fit rSLDS model  
198 describes how neural population activity is expected to evolve over time in the absence  
199 of external perturbation; this can be visualized as a “flow field” of the system. And third,  
200 the “state” of the rSLDS, defined as the linear system that best fits the neural population  
201 activity and dynamics at a given time, can be used to segment neural activity into distinct  
202 regimes in an unsupervised manner, without incorporating any behavioral data. States  
203 identified by rSLDS can subsequently be aligned to behavioral data recorded concurrently  
204 with neural population activity, to determine whether neural states correspond to specific  
205 behavioral bouts or epochs (Supplemental Figure S1A).

206 rSLDS operates under the assumption that a substantial fraction of the observed  
207 variance of recorded neural activity can be captured by a low-dimensional set of latent  
208 variables, which it infers from that activity. We initialized the latent variables using Factor  
209 Analysis, selecting the number of factors for each mouse as the fewest needed to  
210 capture  $\geq 90\%$  of observed variance. The model segments population activity in this low-  
211 dimensional space into a set of discrete states, where the likelihood of the neural  
212 population being in a given state is determined solely by its position in this space (Figure  
213 2A, step ①-②). Linear dynamical systems are fit to the latent variable dynamics within  
214 each discrete state, and model parameters are refined using variational inference to  
215 obtain the final model (Figure 2A, step ③). Each state, defined by its own dynamics matrix,  
216 dictates how the latent variables underlying neural activity evolve in time from any given  
217 point in that particular state space, as well as how that evolution is modified by external  
218 input. Finally, to visualize the fit system, we computed its first two principal components,  
219 and plotted the inferred dynamics in that space either as a flow field, wherein arrows show  
220 the direction and rate of change of activity at each point, or as a 3D landscape, where the

221 rate of change in activity is converted to the height of a 3D landscape (Figure 2A step ④  
222 right).

223 We found that 7-8 latent dimensions could capture 90% ( $7.3 \pm 0.3$ ,  $N=4$  mice) of  
224 observed variance in VMHvl, suggesting that a relatively low-dimensional latent variable  
225 model provided a reasonable approximation of neural activity in this region. In fitting our  
226 model, we set the number of states to be used and the dimensionality of the neural system  
227 that maximized the likelihood of the data, determined using cross validation in each  
228 mouse separately (Supplemental Figure S1B-E). As input to the model, we used the  
229 distance between animals and their facing angle (orientation of the resident towards the  
230 intruder) as a proxy for the strength of social sensory cues (Falkner et al., 2014; Segalin  
231 et al., 2021). This 2D sensory signal is fed as input to the latent variables, scaled linearly  
232 by a fit set of weights to allow each latent variable to be driven to different extents by  
233 external input. Biologically, input to a given latent variable can be interpreted as that input  
234 activating (or inhibiting) the neurons that contribute strongly to that variable.

### 235 **Dynamical systems analysis of VMHvl neural activity reveals an integrator** 236 **dimension that correlates with aggressive escalation**

237 We first examined the dynamics of rSLDS models fit to VMHvl<sup>Esr1</sup> neurons during  
238 encounters with male intruders. Our best fit models required either three or four rSLDS  
239 states; interestingly, attack behavior mostly occurred during a single rSLDS state in all  
240 animals (state 3, Supplementary Figure S1F-H). Attack behavior was not tightly linked  
241 with the onset of this state, but rather the probability of exhibiting attack was elevated  
242 within the state, and on average peaked 20 seconds after the state's onset across animals  
243 (state-triggered average,  $N = 3$  mice, Supplementary Figure S1F<sub>4</sub>). Epochs of the state  
244 enriched for attack also lasted much longer than individual bouts of attack within each  
245 epoch (state 3 epoch duration:  $83.5 \pm 7.5$  seconds, attack bout duration:  $3.66 \pm 0.44$   
246 seconds,  $N = 3$  mice, Supplementary Figure S1F<sub>5</sub>, G<sub>3</sub>, H<sub>3</sub>). In order to better understand  
247 neural population dynamics related to attack behavior, we examined the dynamics matrix  
248 for this state, which describes how neural activity in the latent variable space changes  
249 with time.

250 The eigenvalues of the dynamics matrix reflect the rate at which orthogonal modes  
251 (dimensions) of activity in the system decay to zero following external input, and are  
252 referred to as the time constants of these dimensions (Maheswaranathan et al., 2019;  
253 Strogatz, 2018). External input received along dimensions with short time constants will  
254 quickly decay to zero, whereas input to dimensions with long time constants persists and  
255 decays slowly. Examining the time constants of the dynamics matrix of the attack-related  
256 state revealed a single dimension with an estimated time constant of over 100 seconds  
257 (Figure 2B, Left, red dot). Because systems with long time constants approximately  
258 integrate their input over time, we refer to the longest time constant dimension the  
259 “integration” dimension. Activity along the integration dimension ramped up at the onset  
260 of dominance mounting (a low-intensity aggressive behavior, (Karigo et al., 2021)), and  
261 persisted as the animal attacked (Figure 2B, Right). A single integration dimension, with  
262 a time constant significantly higher than that of the other latent dimensions, could be found  
263 in the rSLDS model for each animal (N=3 mice, Figure 2C). The integration dimension  
264 accounted for  $17.24\% \pm 1.9\%$  of overall variance of neural activity across animals (N = 3  
265 mice). This is significantly higher than the variance explained by an “attack-decoding”  
266 dimension, the dimension obtained by finding a linear projection of the neural population  
267 vector that distinguishes attack from sniffing periods ( $0.5\% \pm 0.1\%$  of variance, N = 3 mice,  
268  $p < 0.001$ , Supplemental Figure S2B) Examining the activity of individual neurons that  
269 were weighted strongly in the integration dimension revealed that around 20% of neurons  
270 per animal showed ramping and persistent activity (Supplemental Figure S2E, F), with  
271 ramping neurons typically but not always preferentially activated by male intruders  
272 (Supplemental Figure S2D). Thus, the ramping dimension reflects a signal that is present  
273 at the level of at least some individual neurons, but is also an emergent property of the  
274 population (Ebitz and Hayden, 2021).

275 To understand what features (if any) the VMHvl integration dimension represented,  
276 we examined its correlation with the animals’ behaviors. We constructed a cumulative  
277 distribution function (cdf) of the level of activation along the integration dimension during  
278 three behaviors: sniffing, dominance mounting, and attack, in all imaged animals. We  
279 found that sniffing consistently occurs at low values of this dimension, dominance mount  
280 at intermediate values, and attack at high values (distribution mean, sniffing: 0.31,

281 dominance mount: 0.67, attack: 0.81, N = 3 mice, **Figure 2E**). This suggests that during  
282 aggressive encounters, neural activity along this dimension grows as animals display  
283 escalating aggressive behaviors. Remarkably, periods of sniffing could be distinguished  
284 from attack or dominance mounting with high accuracy by simply thresholding this one-  
285 dimensional value ( $90.6\% \pm 1.8\%$ , N=3 mice, **Figure 2D**). The same method could also  
286 distinguish low- vs. high-intensity aggressive behavior (i.e., dominance mount vs. attack)  
287 at well above chance accuracy ( $67.3\% \pm 2.9\%$ , N=3 mice). Perhaps due to the slow  
288 dynamics of activity along this dimension, behaviors occurring close together in time, such  
289 as attack and sniff-attack (defined as periods of sniffing that occurred within one second  
290 prior to attack, as described by (Zhu et al., 2020)) could not be distinguished using this  
291 dimension. Remarkably, none of the other eight fit dimensions could be used to  
292 distinguish aggressive behaviors from sniffing with above chance accuracy (**Figure 2F, G**;  
293 **Supplemental Figure S2C**).

294 Because of its slow dynamics, activity in the integration dimension did not decay  
295 between individual bouts of behavior, and could not be used to predict the fine timing of  
296 actions. As a result, we could distinguish pauses (intervals of non-interaction) between  
297 sniffing bouts from pauses between attack bouts with high accuracy ( $83\% \pm 2.1\%$ , N=3  
298 mice), whereas we could not distinguish sniffing bouts from the pauses between them  
299 (**Figure 2D, Supplemental Figure S1A, right, Case 2**). The level of activity along the  
300 integration dimension could not be predicted from the acceleration, facing angle, or  
301 velocity of the resident, or from the distance between the resident and intruder mouse,  
302 suggesting that the dimension did not simply encode pose-related features of the animal  
303 (mean:  $0.35 \pm 0.04 R^2$ , n= 3 mice, **Supplemental Figure S2A**)

304 Thus, our unsupervised approach uncovered a one-dimensional signal in  
305 VMHv<sup>Esr1</sup> neural population activity that closely tracks and scales with an animal's  
306 escalating level of aggressiveness and is reflected in the activity of approximately 20% of  
307 individual VMHv<sup>Esr1</sup> neurons. Different aggressive actions are associated with specific  
308 levels of activity along this dimension, suggesting an aggression-intensity code in  
309 VMHv<sup>Esr1</sup> activity. The fact that few VMHv<sup>Esr1</sup> neurons are tuned for specific aggressive  
310 actions suggests that this intensity code is translated into distinct actions by downstream

311 circuits (Falkner et al., 2020). This correlation between VMHvl<sup>Esr1</sup> activity and aggression  
312 gains additional causal support from the observation that increasing the intensity of  
313 optogenetic stimulation of VMHvl<sup>Esr1</sup> neurons progressively evokes sniffing, dominance  
314 mounting and attack (Lee et al., 2014), actions that can be decoded from the integration  
315 dimension as its activity ramps up.

### 316 **VMHvl contains an approximate line attractor that integrates to create aggressive** 317 **motivation**

318 We next investigated how the fit linear dynamical systems contribute to the overall  
319 dynamics of population activity. For visualization purposes, we used principal component  
320 analysis (PCA) to find the first two principal components (PCs) of the dynamics of the fit  
321 rSLDS model (Figure 3A). In all imaged animals, PC1 showed slow ramping dynamics  
322 that escalated from low activity during the initial phase of social interaction when sniffing  
323 occurred, to higher activity as the animal displayed the first bouts of dominance mounting,  
324 to yet higher activity as the animal switched to attack behavior (Figure 3A, B, PC<sub>1</sub>  
325 (behavior-triggered average, N = 3 mice)). Like the integration dimension in the full rSLDS  
326 space (Figure 2A), activity along PC1 remained persistently high throughout the attack  
327 period, suggesting that the integration dimension is a dominant component of activity in  
328 VMHvl. The component of neural activity along PC2 showed high activity when a new  
329 intruder was introduced but was otherwise low in all animals (Figure 3B, PC<sub>2</sub> (behavior-  
330 triggered average, N = 3 mice)). Together these first two PCs accounted for 69.1%± 1.2%  
331 of the total variance in VMHvl activity across animals (N=3 mice).

332 By identifying the most-likely state of the fit rSLDS model at each point in neural  
333 activity space, we can create a flow field showing how we expect neural dynamics to  
334 evolve within the 2D space spanned by the first two PCs, in the absence of external input.  
335 Doing this revealed a region of low vector flow that forms an approximate line attractor,  
336 meaning that the state of the system tends to move towards points along the line in the  
337 absence of external input (Figure 3C, t<sub>50</sub>-t<sub>340</sub>). Line attractors are powerful coding  
338 mechanisms that allow neural populations to integrate inputs and robustly encode  
339 continuous variables such as head direction or reward value (Ganguli et al., 2008; Hulse  
340 and Jayaraman, 2020; Mante et al., 2013; Seung, 1996). The approximate line attractor  
341 we observed in VMHvl<sup>Esr1</sup> activity is the result of the slow (integration) dimension of our

342 dynamical system. Because all but one pattern of neural activity in the system have  
343 shorter time constants and decay away comparatively quickly, activity evoked by external  
344 sensory perturbations quickly settles into a one-dimensional, slowly decaying pattern.  
345 Continuous sensory or internal input during social interactions produce ongoing  
346 perturbation of the system state in neural activity space, causing it to gradually drift along  
347 the length of the attractor. As activity travels along the approximate line attractor, animals  
348 display a progression of increasingly aggressive behaviors, from sniffing to dominance  
349 mount to attack (Figure 3C, Supplementary Video 1).

350 To visualize better the dynamical landscape of the rSLDS model, we converted the  
351 2D flow field into a 3D landscape, by converting the length of the vector at each position  
352 in neural state space (proportional to the rate of change of activity in the system at that  
353 point; which we term dynamic velocity; see *Methods*) into the height of the landscape  
354 (Figure 3D, E). In this representation, a line attractor appears as a trough or gully,  
355 whereas a point attractor would appear as a locus of stability at the base of a cone (Figure  
356 3D, E, (Seung, 1996)). We observed a dynamic velocity landscape with a trough structure  
357 for every imaged animal (Figure 3F-I, Supplemental Figure S3): the short time constants  
358 of the non-integration dimensions produce the steep walls of the trough (corresponding  
359 to long flow-field arrows), whereas the long time constant of the integration dimension  
360 produces a long, flat gully (corresponding to short flow-field arrows), along which neural  
361 activity slowly evolves (Supplementary Video 2).

362 While the animals' behavior was only strongly correlated with activation along the  
363 integration dimension, it is possible that the rate of change of dynamics in other  
364 dimensions might also show behavior-specific patterns. To test this possibility, we  
365 computed each behavior's 'dynamic velocity': the average length of the vector field across  
366 all dimensions at all time points occupied by a behavior (Figure 3J). We found that time  
367 points associated with entry of the intruder mouse had the highest flows in all animals  
368 and were present on the walls of the trough, while all other behaviors resided within the  
369 base of the trough with little to no flow (Figure 3K). To determine where exactly behaviors  
370 resided along the axis of the trough, we quantified the average normalized value of PC1  
371 for various behaviors across animals. This confirmed that evolution of the system along

372 the trough corresponds with the animal displaying a progressive escalation of aggressive  
373 behaviors and was consistent with our earlier observation of an integration dimension in  
374 VMHvl dynamics (sniff-alone:  $0.24 \pm 0.05$ , dominance-mounting:  $0.56 \pm 0.04$ , attack:  $0.81$   
375  $\pm 0.02$ ,  $N = 3$  mice, **Figure 3L**).

### 376 **The time constant of the integration dimension in VMHvl predicts levels of** 377 **aggressiveness across animals**

378  
379 While imaging from VMHvl in three different mice expressing GCaMP6s always revealed  
380 a single integration dimension with a long time constant, the magnitude of this time  
381 constant varied across animals. Strikingly, we observed a trend in which animals that  
382 displayed more aggressive behavior (calculated as the fraction of time spent attacking)  
383 also exhibited an integration dimension with a longer time constant (**Figure 3M, red points**).  
384 To validate our observation, we performed additional VMHvl<sup>Esr1</sup> imaging in three more  
385 animals using the faster calcium indicator GCaMP7f; we again observed a single  
386 integration dimension in each of the three additional mice (**Figure 3I, Figure 3M yellow**  
387 **points Supplemental Figure S3K-M**). We also re-analyzed VMHvl<sup>Esr1</sup> imaging from three  
388 additional animals from a previous dataset (**Remedios et al., 2017**) where animals  
389 displayed varying amounts of aggressiveness and where GCaMP6s was used as the  
390 calcium indicator (**Figure 3M, purple points**). Remarkably, all nine animals (6 recorded  
391 with GCaMP6s and 3 with GCaMP7f) exhibited a similar relationship between integration  
392 time constant and time spent attacking (**Figure 3M,  $r^2 = 0.79$ ,  $n = 9$  animals**). This striking  
393 correlation of integration time constant with time spent attacking suggests that  
394 aggressiveness may have a neural correlate in the intrinsic dynamics of VMHvl<sup>Esr1</sup>  
395 neurons.

396 To summarize, our unsupervised dynamical systems analysis of Esr1<sup>+</sup> neuronal  
397 population activity in VMHvl identified an approximate line attractor in neural state space,  
398 along which activity evolved with slow ramping dynamics and persistent activity (**Figure**  
399 **3N**). Our analysis further suggests that this nucleus encodes more than just the sex of  
400 the intruder, perhaps reflecting an internal motive state of aggressiveness (**Falkner et al.,**  
401 **2016; Falkner et al., 2020; Remedios et al., 2017**).

402

### 403 **Mating behaviors are represented using rotational dynamics in the MPOA**

404 Since rSLDS was able to discover evidence for integration in VMHvl, we next examined  
405 whether the same analysis would uncover population dynamics important for mating in  
406 MPOA, by fitting models to MPOA<sup>Esr1</sup> neural data from interactions with female intruders  
407 ([Karigo et al. 2021](#)).

408 Fit models of MPOA required three rSLDS states in every animal, with USV+  
409 mounting and intromission mostly occurring in single but different states ([Supplementary](#)  
410 [Figure S4](#)). Unlike in VMHvl, mating behaviors were closely aligned to the onset of  
411 individual neural states, and state bouts were similar to behavior bouts in their duration  
412 ([Supplementary Figure S4 D, E](#)). Upon examining the dynamics matrix associated with  
413 states where mating behaviors such as USV<sup>+</sup> mounting (state 2) occurred in our fit models  
414 of MPOA<sup>Esr1</sup> neurons, we did not find any evidence of dimensions with long time-  
415 constants ([Figure 4A](#)). Instead, the principal components of dynamics in the fit rSLDS  
416 model showed fast dynamics that were highly correlated with the occurrence of specific  
417 behaviors. Across all animals, PC1 of the fit dynamical system showed high activity during  
418 the introduction of a new female intruder, as well as at the onset of individual USV<sup>+</sup>  
419 mounting bouts ([Figure 4B, C](#), behavior triggered average, N = 3 mice), whereas PC2  
420 showed modulation during intromission events ([Figure 4C](#)).

421 The flow-field produced by the model visualized in 2D by PCA revealed that  
422 population activity vector dynamics was dominated by a rotational flow, with neural activity  
423 during a given trial undergoing a series of periodic orbits ([Figure 4D, F](#)). Moreover, the  
424 phase of flow rotation was tightly correlated with the animal's progression through stages  
425 of reproductive behavior (sniffing, mounting, and intromission) ([Figure 4I, J](#) [Supplemental](#)  
426 [Figure S5](#)). Each rotational trajectory corresponded to the sequential activation of  
427 different neurons during different stages of mating ([Figure 4E, G](#), [Supplemental Figure](#)  
428 [S5](#)). This sequential activity was not an artifact of sorting neural activity, as the  
429 sequentiality of the data (seq. index =  $0.22 \pm 0.01$ , N = 3 mice, as defined in [Zhou et al.,](#)  
430 [2020](#)) was significantly greater than shuffled data or random matrices of similar sizes  
431 (shuffle seq. index =  $0.10 \pm 0.002$ , N = 3 mice [Figure 4H](#))

432 We assessed the relationship between the phase of rotational trajectories and  
433 behavior by calculating the angle of rotation aligned to the start of sniffing during mating  
434 episodes (Figure 4I). This revealed that the phase of rotation tracked the sequential  
435 events during a mating cycle, with sniffing, mounting and intromission defined by  
436 characteristic angles of rotation (sniffing:  $18.6^\circ \pm 6.2^\circ$ , mounting:  $79.61^\circ \pm 13.6^\circ$ ,  
437 intromission:  $132.2^\circ \pm 8.1^\circ$ , N = 3 mice Figure 4J). Importantly, rotational dynamics during  
438 mating events were seen in each of the three animals for which we fitted rSLDS models  
439 (Supplemental Figure S5). The dynamic velocity associated with behaviors in MPOA  
440 revealed high flows associated with consummatory behaviors, which was markedly  
441 different from the slow dynamics during aggressive behavior in VMHvl (Figure 3L, 4K).

442 Thus, unlike the slow ramping dynamics identified in VMHvl, rSLDS discovered  
443 faster, behaviorally time-locked rotational dynamics in MPOA. Furthermore, we found that  
444 during mating bouts, MPOA exhibits sequential activation of a series of neurons, whose  
445 firing is aligned with distinct stages of the behavior (Figure 4L).

#### 446 **Distinct neural coding schemes for similar behavior in VMHvl vs MPOA**

447 Our dynamical systems analysis of social behavior in VMHvl and MPOA identified two  
448 distinct neural coding schemes for aggression vs mating behavior in the two nuclei. The  
449 integration dimension found in VMHvl is strikingly absent in MPOA, emphasizing the slow  
450 ramping nature of dynamics in VMHvl compared to the fast behaviorally aligned dynamics  
451 in MPOA (Figure 5A, B). Behaviors such as attack occur during periods with relatively  
452 small rates of change in VMHvl population dynamics, and the system resides within the  
453 trough of a dynamic velocity landscape. In contrast, consummatory behaviors in MPO  
454 have high rates of change in population dynamics, due to the rotational nature of the  
455 system (Figure 5C, D). Yet both regions possess a signal that tracks aggressive and  
456 mating behavior: the value of the integration dimension in VMHvl is correlated with  
457 escalating aggressive behavior, while the angle of rotational dynamics in MPOA is  
458 correlated with progression of mating episodes (Figure 5E, F). The rotational dynamics in  
459 MPOA are accompanied by sequential activation of individual neurons, while sequential  
460 activity is absent during aggression episodes in VMHvl (Figure 5G, H).

461 Thus the same method, rSLDS, uncovers two distinct forms of dynamics for encoding  
462 similar social behavior in VMHvl and MPOA (Figure 5I, L).

### 463 **VMHvl also contains an integrator dimension encoding reproductive state**

464 Our discovery of line attractor dynamics for aggression in VMHvl and rotational dynamics  
465 for mating in MPOA raised an important question: do these contrasting dynamics reflect  
466 fundamental properties of aggressive vs. mating behavior, or do they reflect differences  
467 in the functional roles of the two nuclei with respect to social behaviors? To address this,  
468 we fit models to neural activity from VMHvl<sup>Esr1</sup> neurons during social interactions with  
469 females.

470 Fit models required three rSLDS states in all animals, with mating behaviors (USV+  
471 mounting and intromission) mostly present in one state (state 3, Supplementary Figure  
472 S6A-H). As in the case of aggression, bouts of the mating-dominant state in VMHvl lasted  
473 much longer than individual bouts of mating behavior (Supplementary Figure S6D, H).  
474 Given the persistence of the mating states discovered by rSLDS in VMHvl, we examined  
475 the time constants associated with each dimension of the mating-dominant state in VMHvl  
476 (state 3, Supplementary Figure S6). As for aggression, we found a single integration  
477 dimension with ramping and persistent activity, with a large time constant in every animal  
478 (Figure 6A red dot, 6B). We next asked if we could distinguish mating vs non-mating  
479 behavior from the value of this single dimension. Surprisingly, we could distinguish pairs  
480 of behaviors with high accuracy (intromission vs sniffing:  $0.94 \pm 0.02$  N = 2 animals (third  
481 animal did not display intromission), USV<sup>+</sup> mounting vs sniffing:  $0.78 \pm 0.04$  N = 3 animals  
482 Supplementary Figure S6I). As for aggression, we could distinguish periods of non-  
483 interaction between mounting bouts from those between sniffing bouts (Supplementary  
484 Figure S6I), but could not distinguish sniff-mount (sniffing occurring within one second of  
485 mounting) from mounting. Finally, the cumulative distribution of the value of the  
486 integration dimension during sniffing, mounting, or intromission revealed that sniffing  
487 occurs at the lowest values of this dimension, USV<sup>+</sup> mounting occurs at intermediate  
488 values, while intromission occurs at the highest values of this dimension (Figure 6C). All  
489 of these analyses indicate that the dynamics of VMHvl during reproductive behavior  
490 closely resemble those observed in VMHvl during aggression.

491 To continue our comparison, we projected our high dimensional model into a two-  
492 dimensional space using PCA (Figure 6D). The resulting projections appeared similar to  
493 those seen in VMHvl during aggressive encounters with males. PC1 had low activity  
494 during sniffing bouts, with activity ramping up as early USV<sup>+</sup> mounting (typically not  
495 proceeding to intromission) was displayed, and remaining persistently high for hundreds  
496 of seconds as the animal showed several cycles that progressed from sniffing to mounting  
497 to intromission (Figure 6D). Conversely, PC2 showed high activity during the introduction  
498 of a new intruder but was otherwise low. Examining the underlying vector field revealed  
499 regions of stability in mating-related states that resembled an approximate line attractor  
500 and a trough shaped dynamic velocity landscape, with neural activity moving along the  
501 line attractor as the animal progressed from the appetitive to consummatory phases of  
502 mating (Figure 6E, F); apparent rotations in Figure 6E occurred only when introduction of  
503 a new intruder transiently increased activity along PC2. Across animals, dynamic velocity  
504 analysis revealed that only times of intruder introduction had high flows, while all other  
505 behaviors had little flow and were present in the trough of the dynamic velocity landscape  
506 (Figure 6G).

507 Lastly, examining the weighted activity of neurons that contribute to the integration  
508 dimension revealed several cells with ramping and persistent activity during male-female  
509 encounters (Supplementary Figure S6J). The integration dimension seen during mating  
510 behavior was biased towards neurons tuned to female intruders, and was largely non-  
511 overlapping with neurons that created the aggressiveness integration dimension seen in  
512 interactions with males (Supplementary Figure S6F).

513 Thus, the application of rSLDS to data recorded during male-female social  
514 interactions uncovered a representation of mating in VMHvl in which activity evolves  
515 along a line attractor, possibly reflecting the intensity of reproductive drive. This attractor  
516 is similar to that found in VMHvl during aggression, but incorporates primarily female-  
517 selective rather than male-selective neurons (Figure 6H, I). In contrast, behavior-locked  
518 rotational dynamics like those found in MPOA during mating behavior were not observed  
519 in VMHvl. We therefore conclude that line-attractor dynamics are a general feature of  
520 VMHvl, rather than a signature of a particular type of social behavior.

## 521 Discussion

522 The dramatic and specific behavioral phenotypes obtained by optogenetically activating  
523 genetically distinct hypothalamic neuronal cell classes has supported the idea that the  
524 hypothalamus controls innate behaviors via dedicated, behavior-specific neural subsets.  
525 This conclusion has also been drawn from c-fos labeling experiments performed in  
526 combination with transcriptomic identification of hypothalamic cell types in the pre-optic  
527 area (POA), which has revealed neuronal subtypes selectively activated during parental,  
528 reproductive or aggressive behaviors (Moffitt et al., 2018). In MPOA, moreover, different  
529 subsets of neurons have been shown to project to distinct downstream targets, with  
530 minimal collateralization (Kohl et al., 2018). Together, these data have reinforced the  
531 prevailing view that hypothalamic nuclei are comprised of genetically specified, behavior-  
532 specific neuronal subpopulations connected in developmentally determined pathways or  
533 “labeled lines” (Ishii et al., 2017; Kohl et al., 2018).

534 It is tempting to generalize these findings to other hypothalamic nuclei that control  
535 different survival behaviors. Indeed, studies of the arcuate nucleus (ARC) have revealed  
536 genetically distinct subpopulations that control feeding behavior via non-collateralizing  
537 projections to different targets (Stenerson, 2013). Like MPOA, moreover, ARC is  
538 predominantly GABAergic. However, other behaviorally relevant hypothalamic nuclei  
539 exhibit very different neurochemical, cytoarchitectonic and connectional features. For  
540 example, VMHvl and PMv, which play a dominant role in the control of aggression (Lee  
541 et al., 2014; Lin et al., 2011; Stagkourakis et al., 2018; Yang et al., 2013), are  
542 predominantly glutamatergic, with a surrounding GABAergic “shell.” Furthermore,  
543 VMHvl<sup>Esr1</sup> neurons collateralize extensively to their downstream targets (Lo et al., 2019),  
544 unlike MPOA and ARC (Figure 1B). Finally, unlike the case in the POA (Moffitt et al.,  
545 2018), immediate early gene expression and scRNAseq analysis in VMHvl has failed to  
546 reveal a robust relationship between transcriptomic cell type identify and behavior-specific  
547 activation (Kim et al., 2019). The functional significance of these differences between  
548 MPOA and VMHvl has until now remained unclear.

549

550 **MPOA and VMHvl encode social behaviors in a digital vs. analog manner,**  
551 **respectively**

552 Here we report that MPOA<sup>Esr1</sup> and VMHvl<sup>Esr1</sup> neurons utilize very different schemes for  
553 the neural coding of behavior, despite the fact that optogenetic stimulation of these  
554 neurons evokes mating and aggression, respectively, two highly related social behaviors.  
555 GCaMP imaging of VMHvl<sup>Esr1</sup> neurons during social interactions has revealed very few  
556 cells tuned to specific behavioral actions, unlike the case in MPOA in which many neurons  
557 are only active during a specific preferred behavior (Karigo et al., 2021; Remedios et al.,  
558 2017). In contrast, we show that specific aggressive behaviors can be decoded from  
559 features of population neural activity in VMHvl. Thus, MPOA represents behavior via a  
560 cell identity code, while VMHvl does so via a population code.

561 Our studies here reveal the nature of this population code. rSLDS analysis of  
562 VMHvl neural activity during male-male social interactions, projected by rSLDS into an 8-  
563 dimensional latent factor space, revealed one dimension with a long time-constant that  
564 exhibits progressively increasing activity during escalating aggressive encounters.  
565 Different aggressive actions, such as dominance mounting or attack, can be distinguished  
566 with high accuracy by the neural activity along this single dimension. In a topological  
567 representation, these dynamics can be visualized as a progression along a stable “trough”  
568 or gully, which has the characteristics of a line attractor. In contrast, a similar analysis of  
569 MPOA revealed rotational dynamics, in which the population cycles through distinct states  
570 generated by the activity of behavior-specific cell types during each bout of mating. Put  
571 simply, VMHvl coding of behavior appears to be analog, while MPOA coding of behavior  
572 appears more digital.

573 The different neural codes for behavior we have uncovered in VMHvl and MPOA  
574 fit well with their distinct neurochemical and cytoarchitectonic features. Glutamatergic  
575 neurons in VMHdm exhibit local connectivity (Kennedy et al., 2020) which, if true for  
576 VMHvl as well, can in theory support the persistent activity necessary for the ramping  
577 activity and attractor dynamics we observe. Conversely, the fact that the majority (85%)  
578 of MPOA neurons (including those that control mating) are GABAergic could provide a  
579 substrate for reciprocal inhibitory connections between action-specific subpopulations.

580 Such connectivity could produce winner-take-all dynamics or feed-forward dis-inhibitory  
581 circuits that control transitions between sequential action phases of mating (e.g., from  
582 mounting to intromission), giving rise to the rotational dynamics observed in neural data.  
583 The existence of such circuits in MPOA can be investigated using slice physiology or in  
584 vivo imaging experiments once appropriate cell type-specific markers become available.

585 Why should MPOA and VMHvl utilize such different strategies for the coding of  
586 closely related social behaviors? It is tempting to attribute this difference in population  
587 dynamics to distinct features of reproductive vs aggressive behavior. For example,  
588 aggressive encounters can dynamically escalate or de-escalate, in order to avoid serious  
589 injury or death to the combatants, whereas male mating typically proceeds to completion  
590 (ejaculation) once initiated. These differences are well-suited to control by ramping and  
591 cycling neuronal dynamics, respectively. In this view, the different properties and coding  
592 strategies of VMHvl and MPOA may have evolved to be optimally adaptive for fighting  
593 and mating, respectively.

594 However, our analysis also revealed line attractor dynamics in the subset of  
595 VMHvl<sup>Esr1</sup> neurons that is female-tuned and active during mating ([Remedios et al., 2017](#)).  
596 This suggests that line attractor dynamics are a general property of behavioral coding by  
597 VMHvl, not an aggression-specific feature. By the same token, MPOA contains specific  
598 neurons highly tuned to attack, in contrast to VMHvl (although it is not yet clear whether  
599 these neurons play an aggression-promoting or –inhibiting role). Thus, our analysis  
600 suggests that MPOA and VMHvl more likely encode different aspects of mating behavior,  
601 such as action selection vs. drive state intensity, respectively. A generalization of this view  
602 predicts that the hypothalamus should contain at least one additional nucleus with MPOA-  
603 like behavioral coding, which controls aggression. Indeed, the anterior hypothalamic  
604 nucleus (AHN), which has a similar neurochemical and cytoarchitectonic structure as  
605 MPOA, can promote defensive attack ([Nelson and Trainor, 2007](#); [Xie et al., 2022](#)); it will  
606 be interesting to see whether rotational dynamics are observed in this structure.  
607 Conversely, this view predicts that PMv, which promotes aggression and is primarily  
608 glutamatergic like VMHvl ([Stagkourakis et al., 2018](#)), may utilize population coding of  
609 behavior and exhibit line attractor dynamics.

## 610 **Potential functions of the VMHvl line attractor**

611 Line attractors have been identified in cortical and hippocampal regions involved in  
612 cognitive functions, such as decision-making, spatial mapping and sensory discrimination.  
613 It is unexpected to find such neural dynamics in the hypothalamus, which is widely viewed  
614 as controlling innate behaviors via action-specific cell types similar to those observed in  
615 MPOA. What function(s) might such attractor dynamics serve, in the context of innate  
616 behaviors? Two explanations are possible, which are not mutually exclusive.

617         First, progression along the line attractor may encode the intensity of an internal  
618 motive state of aggressiveness. This is supported by our finding that the integration  
619 dimension that contributes to this attractor can distinguish periods of non-social  
620 interaction during high- vs. low-intensity phases of aggressive escalation (**Figure 2D**). In  
621 this view, the line attractor functions to maintain the system in a stable motive state, during  
622 variable behavior. Note that this line attractor traverses the boundary between two of the  
623 linear dynamic states identified by rSLDS (**Figure 3C**). Therefore, the brain state of  
624 aggressiveness is a property of the overall dynamics of VMHvl population activity, not just  
625 of one rSLDS “state”. The idea that an internal emotion or motive state may be encoded  
626 by a continuous line attractor provides a way to stably maintain such a state, whether or  
627 not its associated behaviors are overtly expressed on a moment-to-moment basis. The  
628 neural mechanisms that underly this state could include recurrent excitatory networks,  
629 neuromodulatory systems or a combination of both, as observed in VMHdm neurons  
630 controlling a fear-like state (**Kennedy et al., 2020**).

631         An alternative explanation is that the line attractor may serve as an integrator that  
632 accumulates “evidence” used to make behavioral decisions, such as the decision to  
633 switch from sniff to dominance mount, or from dominance mount to attack. Such a function  
634 would require that different behaviors be triggered at different threshold values of the  
635 integrator. This type of ramp-to-threshold mechanism has been suggested to control  
636 sequential actions during male courtship behavior in *Drosophila* (**McKellar et al., 2019**)  
637 and predator escape in mice (**Evans et al., 2018**). These two functions are not  
638 incompatible: the attractor could encode both the intensity of an internal state, and  
639 (indirectly) the selection of actions at different state intensities.

640 Finally, line attractor dynamics could serve useful functions in the context of  
641 behavioral plasticity and individual variation. For example, VMHvl<sup>Esr1</sup> neurons show  
642 increased selective tuning for male vs. female intruders as a function of social experience  
643 ([Remedios et al., 2017](#)), and exhibit a form of long-term potentiation that underlies the  
644 increase in aggressiveness that occurs when mice win a series of fights ([Stagkourakis et  
645 al., 2020](#)). It will be interesting to determine whether changes in flow field dynamics or  
646 attractor properties are associated with these forms of experience-dependent plasticity.  
647 Finally, we note that differences in line attractor properties were observed among mice  
648 which exhibited different and characteristic levels of aggressiveness ([Figure 3M](#)). It is  
649 possible that individual differences in aggressiveness may reflect, or be caused by,  
650 individual constraints on population dynamics in VMHvl.

### 651 **Computational vs. behavioral measurements of internal brain states**

652 Traditional approaches to identifying internal drive or motivational states have relied on  
653 learned behavioral tests such as operant conditioning. Neural activity that correlates with  
654 the execution and intensity of the conditioned instrumental behavior (e.g., bar-pressing),  
655 as determined using Progressive Ratio experimental designs, is interpreted as encoding  
656 the motivational state and its relative strength ([Atasoy et al., 2012](#)). While this approach  
657 has worked well for homeostatic motivational states such as hunger and thirst, there are  
658 several problems with generalizing it to innate social behaviors. First, it cannot be applied  
659 while the animal is directly engaged in a behavior such as aggression, because it requires  
660 the animal to cease directing its behavior towards the conspecific and to re-direct it  
661 towards the conditioning apparatus (nose-poke or bar-press). Therefore, it can be used  
662 to measure an animal's motivational drive to seek out the opportunity to engage in a social  
663 behavior ([Covington et al., 2019](#); [Falkner et al., 2016](#); [Golden et al., 2019](#)), but not its  
664 state during engagement in the social behavior *per se*. Second, it substitutes the  
665 performance of a learned, artificial (instrumental) behavior for that of an innate behavior.  
666 Finally, it restricts the analysis of neural correlates of the motivational state to recordings  
667 performed occurs during the performance of the instrumental behavior.

668 Here, we have identified neural correlates of aggressive and mating internal drive  
669 states by examining the dynamic landscape of population neuronal activity in VMHvl. This

670 approach does not require any instrumental operant conditioning, but can be performed  
671 on data recorded during the naturalistic behavior itself. Moreover, the approach identifies  
672 the states purely from analysis of neural population activity, without any reference to  
673 behavioral annotation. Importantly, unlike neural correlates of operant conditioning which  
674 are observed during performance of the instrumental behavior (Falkner et al., 2016), the  
675 signal discovered by rSLDS analysis can be observed both when the animal is behaving,  
676 and when it is not behaving (i.e., during inter-bout pauses). Indeed, it is the persistence  
677 of this signal throughout both active attack behavior and intermittent periods of inactivity  
678 between attack bouts, that suggests it encodes an internal state rather than behavior itself  
679 (Figure S1A). That this persistence is not due to slow GCaMP dynamics is suggested by  
680 the fact that 1) it is not observed in MPOA; and 2) it is also observed using a faster version  
681 of GCaMP (7f).

682 Our conclusion that VMHvl<sup>Esr1</sup> neurons in males encode an internal motive or drive  
683 state underlying aggression, rather than simply the sex identity of a conspecific male, is  
684 consistent with recent studies of this neuronal population in female mice. Unlike male  
685 mice, which only attack other males, lactating female mice attack intruders of both sexes.  
686 A subset of VMHvl<sup>Esr1</sup> neurons in females that express the GPCR gene *Npy2r*, called  $\beta$   
687 cells, are both necessary for maternal aggression and sufficient to promote attack in non-  
688 aggressive virgin females (Liu et al., 2022). Bulk calcium measurements in behaving  
689 animals show that  $\beta$  cells are equally active during maternal aggression towards both  
690 male and female intruders. However, these cells display lower activity in individual mice  
691 that are non-aggressive (Liu et al., 2022). These data suggest that VMHvl<sup>Esr1</sup>  $\beta$  cells in  
692 females encode aggressiveness rather than intruder sex; the same may be true for males.

### 693 **Testable predictions of the line-attractor model**

694 Our rSLDS model of VMHvl dynamics makes several testable predictions and raises  
695 several interesting questions for future investigation. First, it predicts that once in the  
696 attractor, the system will return quickly to it following perturbations that move it out of this  
697 stable trough. This behavior is suggested by the brief excursion out of the attractor that  
698 occurs when a first intruder is removed and replaced by a second one. However, it would  
699 be ideal to demonstrate this directly by transiently activating neurons that contribute to

700 the attractor, and determining whether the system rapidly returns to it following stimulus  
701 offset, as has been demonstrated for point attractors underlying working memory in ALM  
702 (Inagaki et al., 2019). Another prediction is that selectively inactivating the VMHvl<sup>Esr1</sup>  
703 neurons that exhibit slow dynamics should eliminate the line attractor. Such experiments  
704 will require combined optogenetic perturbations and calcium imaging in this deep  
705 subcortical structure.

706 Single-cell RNAseq experiments have shown that the Esr1<sup>+</sup> population in VMHvl  
707 contains 6-7 distinct transcriptomic subtypes (Kim et al., 2019). An interesting question is  
708 whether all, or just a subset, of these cell types contribute to attractor dynamics. This  
709 question can be addressed once genetic drivers that are specific for these subtypes are  
710 generated. An additional question is whether the slow dynamics observed for some  
711 VMHvl<sup>Esr1</sup> neurons reflects recurrent connectivity between them, as has been  
712 demonstrated for fear-encoding neurons in VMHdm (Kennedy et al., 2020), or the release  
713 of slow-acting neuromodulators such as neuropeptides. Recurrent connectivity in VMHvl  
714 can be investigated by slice electrophysiology and ultimately by EM connectomics.  
715 VMHvl<sup>Esr1</sup> neurons are known to express multiple neuropeptides, as well as receptors for  
716 neuropeptides and other neuromodulators. New sensors for detecting neuromodulator  
717 release (Sabatini and Tian, 2020; Sun et al., 2018), as well as methods for selectively  
718 perturbing neuromodulator function while simultaneously imaging population neural  
719 activity *in vivo*, should help to address these questions in the future.

## 720 **Evolutionary implications**

721 The observation that neural activity in MPOA during social behavior reflects distinct  
722 subpopulations, whose activity is time-locked to specific behavioral actions, is consonant  
723 with the prevailing view that the hypothalamus encodes innate behaviors via  
724 developmentally determined cell types with hard-wired connectivity (Ishii et al., 2017; Kohl  
725 et al., 2018; Moffitt et al., 2018). In contrast, the mixed selectivity exhibited by VMHvl  
726 neurons is more often observed in the cortex (Fusi et al., 2016) where attractor dynamics  
727 have also been identified as a component of population coding. As in the cortex, coding  
728 in VMHvl is mediated predominantly by glutamatergic neurons, with GABAergic neurons  
729 in the shell apparently playing a more peripheral role, whereas in the MPOA behavioral

730 control is carried out predominantly by GABAergic projection neurons (Chen et al., 2021;  
731 Karigo et al., 2021), similar to the basal ganglia (Graybiel, 2000; Klaus et al., 2019; Park  
732 et al., 2020). As the hypothalamus emerged in vertebrate evolution long before the cortex,  
733 it is tempting to speculate that VMHvl and related glutamatergic nuclei might have  
734 functioned like a primitive cortex, while MPOA and related GABAergic nuclei might have  
735 functioned analogously to the basal ganglia. Comparative studies of hypothalamic neural  
736 population dynamics in non-traditional model organisms may help to shed light on this  
737 hypothesis.

### 738 **Acknowledgments**

739 We thank S. Ganguli and M. Schnitzer for discussions on conceptualizing this project at  
740 its inception. We thank H. Inagaki and L.F. Abbott for critical feedback on this manuscript,  
741 C. Chiu for laboratory management and G. Mancuso for administrative assistance, and  
742 members of the Anderson and Kennedy labs for helpful comments on this project. A. N.  
743 is supported by a National Science Scholarship from the Agency of Science, Technology  
744 and Research, Singapore. D.J.A. is an Investigator of the Howard Hughes Medical  
745 Institute. A.K. is supported by NIH R00MH117264. The content is solely the responsibility  
746 of the authors and does not necessarily represent the official views of the National  
747 Institutes of Health.

### 748 **Author contributions**

749 D.J.A, A.K and A.N conceived of the project and wrote the manuscript, with input from  
750 T.K, B.Y and S.L. A.K performed the clustering analysis of single neurons and A.N  
751 performed all dynamical system modelling.

752

753

754

755

756

## 757 **Figure Legends**

### 758 **Figure 1: Cytoarchitectures and cellular representations in a neural system** 759 **regulating social behavior**

760 A: cytoarchitecture of the MPOA. B: cytoarchitecture of the VMHvl. C: neural imaging  
761 studies of *Esr1*+ neurons in the MPOA find neurons tuned to mounting behavior. D: neural  
762 imaging studies of *Esr1*+ in the VMHvl find few if any neurons tuned to aggressive  
763 behavior. E: clustering of recorded *Esr1*+ neurons in MPOA using a regression model  
764 reveals many populations of behavior-tuned neurons (n =306 neurons from 3 mice). F:  
765 clustering of recorded *Esr1*+ neurons in VMHvl using a regression model reveals that  
766 most neurons are tuned to the sex of the intruder and few neurons are tuned to any  
767 behavior (n = 391 neurons from 4 mice).

### 768 **Figure 2: Dynamical analysis of VMHvl neural activity reveals an integrator** 769 **dimension that correlates with aggressive escalation**

770 A: application of recurrent switching linear dynamical systems (rSLDS) to neural data  
771 obtained from the MPOA or VMHvl. B: time constants of dynamics matrix of attack  
772 enriched state from example VMHvl mouse 1. The red dot highlights the largest time  
773 constant or integration dimension. C: Time constant from all animals arranged in  
774 decreasing order. The integration dimension (dim 1) is significantly larger than all other  
775 dimension ( $p < 0.001$ , n = 3 mice). D: decoding behaviors from integration dimension (\*\*p  
776 < 0.005, \*p<0.01, n = 3 mice). E: empirical cumulative distribution of value of integration  
777 dimension (normalized) for various behaviors. F: temporal dynamics of fastest dimension  
778 in example VMHvl mouse 1. G: decoding behaviors from fastest dimension across  
779 animals (n = 3 mice).

### 780 **Figure 3: VMHvl contains an approximate line attractor that integrates to create** 781 **aggressive motivation**

782 A: state and behavior rasters shown with principal components of latent factors for  
783 example VMHvl mouse 1. B: behavior triggered average of top two principal components  
784 aligned to intruder introduction or first attack onset (n = 3 mice). C: neural state space  
785 with population trajectories for VMHvl mouse 1 colored by behaviors performed by the

786 resident mouse. The inferred flow field of the model is shown behind trajectories. D,E:  
787 inferred dynamics shown as a dynamic velocity landscape, where the size (scalar value)  
788 of flow field vectors is represented as the height of the 3D landscape. F,G: inferred  
789 dynamic velocity landscape in VMHvl mouse 1. H: inferred dynamic velocity landscape  
790 for VMHvl mouse 3. I: inferred dynamic velocity landscape from a separate mouse where  
791 GCaMP 7f was used, showing a similar trough shaped landscape. J: calculation of  
792 dynamic velocity: the average vector length across dimensions for all time points of a  
793 given behavior. K: quantification of dynamic velocity (n = 3 mice, \*\*\*p<0.001). L: position  
794 of various behaviors along trough, i.e PC1 in neural state space (n = 4 mice, \*\*p<0.005,  
795 \*p<0.01). M: relationship between the time spent attacking and the time constant of the  
796 integration dimension ( $r^2$ : 0.79, n = 9 animals; orange points are data from [Karigo et al.,](#)  
797 [2021](#), purple points are data from [Remedios et al., 2017](#), yellow points are data from [Yang](#)  
798 [& Anderson, 2022](#)). N: dynamical analysis finds an integration dimension that functions  
799 as an approximate line-attractor encoding an aggressive-intent drive in VMHvl.

800 **Figure 4: Mating behaviors are represented using rotational dynamics in the MPOA**

801 A: time constants from dynamics matrix of mating behavior-enriched state in MPOA (n =  
802 3 mice) B: state and behavior rasters shown with principal components of latent factors  
803 for example MPOA mouse 1. C: behavior triggered average of top two principal  
804 components aligned to USV+ mount onset and intromission onset (n = 3 mice). D: neural  
805 state space with rotational population trajectories from mating episodes shown in E of  
806 MPOA mouse 1, colored by behaviors performed by resident mouse. E: sequential activity  
807 of MPOA neurons during mating episodes whose rotational population trajectories are  
808 shown in D. F,G: same as D,E but for MPOA mouse 2. H: quantification of sequential  
809 index for MPOA (n = 3 mice, \*\*\*p<0.001). I: calculation of angle of rotation ( $\theta$ ) aligned to  
810 the start of sniffing during mating episodes (top). Empirical cumulative distribution of  $\theta$  for  
811 various behaviors (n = mice, bottom). J: quantification of  $\theta$  for various mating behaviors  
812 (n = 3 mice, \*\*\*p<0.001, \*\*p<0.005, \*p<0.01, top). Schematic depicting  $\theta$  for mating  
813 behaviors (bottom). K: quantification of dynamic velocity for mating behavior in MPOA (n  
814 = 3 mice). L: dynamical analysis in MPOA find behaviorally tuned factors that displays a  
815 rotational encoding of actions.

816 **Figure 5: Distinct neural coding schemes for similar behavior in VMHvl vs MPOA**

817 A: time constants from dynamics matrix of attack behavior-enriched state in VMHvl (n =  
818 3 mice), reproduced from Figure 2C. B: time constants from dynamics matrix of mating  
819 behavior-enriched state in MPOA (n = 3 mice), reproduced from Figure 4A. C,D:  
820 quantification of dynamic velocity in VMHvl (C) and MPOA (D). Reproduced from Figure  
821 3K and Figure 4K resp. E: empirical cumulative distribution of value of integration  
822 dimension (normalized) in VMHvl for various behaviors, reproduced from Figure 2E. F:  
823 empirical cumulative distribution of angle of rotation (normalized) in MPOA for various  
824 behaviors , reproduced from Figure 4I. G: Sequentiality index in MPOA (n = 3 mice),  
825 reproduced from Figure 4E. H: Sequentiality index in VMHvl in aggression (n = 3 mice).  
826 I: dynamical analysis finds an integration dimension that functions as an approximate line-  
827 attractor encoding an aggressive-intent drive in VMHvl. J: dynamical analysis in MPOA  
828 find behaviorally tuned factors that displays a rotational encoding of actions.

829 **Figure 6: VMHvl contains a separate approximate line attractor encoding**  
830 **reproductive intent**

831 A: time constants of dynamics matrix of mating enriched state from example VMHvl  
832 mouse 1. The red dot highlights the largest time constant or integration dimension. B:  
833 Time constant from all animals arranged in decreasing order. The integration dimension  
834 (dim 1) is significantly larger than all other dimension ( $p < 0.001$ , n = 3 mice). C: empirical  
835 cumulative distribution of value of integration dimension (normalized) for various  
836 behaviors. D: state and behavior rasters shown with principal components of latent factors  
837 for example VMHvl mouse 1. E: neural state space with population trajectories for VMHvl  
838 mouse 1 colored by behaviors performed by the resident mouse. The inferred flow field  
839 of the model is shown behind trajectories. F: dynamic velocity landscape with population  
840 trajectory colors by behavior. G: quantification of dynamic velocity during mating behavior  
841 in VMHvl across animals ( $p < 0.001$ , n = 3 mice). H: MPOA contains distinct cell  
842 populations that are organized by rotational dynamics and encodes actions. I: VMHvl  
843 contains mixed selective neurons that are organized by line attractor dynamics that  
844 encode a representation of escalating motivational states.

845

## 846 **Methods**

### 847 **Data**

#### 848 **Neural imaging data (Karigo et al., 2021, Remedios et al., 2017, Yang and** 849 **Anderson, 2022)**

850 We analyzed data from three sets of previous experiments (Karigo et al., 2021; Remedios  
851 et al., 2017; Yang and Anderson, 2022) All experiments were approved by the Institute  
852 Animal Care and Use Committee (IACUC) and the Institute Biosafety Committee (IBC) at  
853 the California Institute of Technology (Caltech). Briefly, for data obtained from Karigo et  
854 al., 2021, *Esr1<sup>cre</sup>* knock-in mice, in which GCaMP6s was expressed selectively in *Esr1*  
855 neurons in either the medial preoptic area (MPOA) or the ventrolateral subdivision of the  
856 ventromedial hypothalamus (VMHvl), were allowed to interact with BALB/c male and  
857 female intruders in a standard resident intruder assay (cite). Male or female intruders  
858 were introduced into the home case in a random order, with a 5-10 min interval between  
859 intruder session. Each session typically lasted 10-20 minutes. Behavior videos of  
860 interacting animals were annotated using a custom MATLAB-based interface. A total of  
861 7 behaviors including sniffing, dominance-mount, attack, mount, intromission, interact  
862 (periods where animals were close to each other but other behaviors were absent) were  
863 annotated with male and female intruders. A head-mounted micro-endoscope was used  
864 to acquire Ca<sup>2+</sup> imaging data at 15Hz from either MPOA<sup>Esr1</sup> neurons (total of 583 neurons  
865 from 3 mice) or VMHvl<sup>Esr1</sup> neurons (total of 421 neurons from 3 mice) for neural data  
866 analysis described in sections below.

867 For data obtained from Yang and Anderson, 2022, briefly, *Esr1<sup>cre</sup>* knock-in mice, in which  
868 GCaMP7f was expressed selectively in *Esr1* neurons in VMHvl, were allowed to interact  
869 with BALB/c male intruders in a standard resident intruder assay. In addition to the  
870 behaviors annotated for above, male intruders were also “dangled”, where the ano-genital  
871 region of the dangled intruder is held next to the resident mouse. A head-mounting micro-  
872 endoscope was used to acquire Ca<sup>2+</sup> imaging data at 30Hz from VMHvl<sup>Esr1</sup> neurons (386  
873 neurons from 3 mice) for neural data analysis described in sections below.

874 For data obtained from [Remedios et al, 2017](#), briefly, *Esr1<sup>cre</sup>* knock-in mice, in which  
875 GCaMP6s was expressed selectively in *Esr1* neurons in VMHvl, were allowed to interact  
876 with BALB/c male intruders in a standard resident intruder assay. A head-mounting micro-  
877 endoscope was used to acquire Ca<sup>2+</sup> imaging data at 30Hz from VMHvl<sup>Esr1</sup> neurons (358  
878 neurons from 3 mice) for neural data analysis described in sections below.

## 879 [Neural data analysis](#)

### 880 **Tuning rasters for single neurons**

881 We examined the tuning properties of single neurons in VMHvl<sup>Esr1</sup> or MPOA<sup>Esr1</sup> by  
882 creating behavior tuning rasters (Figure 1 C, D). We first computed the mean activity of  
883 each neuron for each the 14 manually annotated behavioral actions. To group neurons,  
884 we created a set of 40 regressors representing combinations of behavioral actions, and  
885 grouped neurons by which single regressor captured the most variance in each cell's  
886 activity. In addition to regressors for individual behaviors, example regressors include  
887 signals such as all male-directed actions, all female-directed actions, all male-  
888 directed/female-directed/sex-invariant investigative behaviors, and all male-  
889 directed/female-directed/sex-invariant consummatory behaviors. Neurons for which no  
890 single regressor captured at least 50% of variance in behavior-averaged activity were  
891 omitted from the visualization (approximately 5% of cells.)

### 892 **Computation of pose features for input to dynamical model**

893 As external input to the dynamical model (see next section), we selected two features of  
894 animal pose estimates produced by the Mouse Action Recognition System (MARS,  
895 [Segalin et al., 2020](#)) The first of these is the distance between animals, computed as the  
896 distance between centroids of ellipses fit to the poses of the two mice. The second is the  
897 facing angle of the resident towards intruder mouse, defined as the angle between a  
898 vector connecting the centroids of the two mice and a vector from the centroid to the nose  
899 of the resident mouse.

900

901

## 902 **Dynamical system models of neural data**

903 We model neural activity using a recurrent switching linear dynamical systems (rSLDS)  
904 according to previous methods (Linderman et al, 2019, Linderman et al., 2017). Briefly,  
905 rSLDS is a generative model that breaks down non-linear time series data into sequences  
906 of linear dynamical modes. The model relates three sets of variables: a set of discrete  
907 states ( $z$ ), a set of continuous latent factors ( $x$ ) that captures the low-dimensional nature  
908 of neural activity, and the activity of recorded neurons ( $y$ ). The model also allows for  
909 external inputs ( $u$ ), for which we used the two pose features described in the previous  
910 section. The between these various levels is shown graphically in [Supplementary Figure](#)  
911 [13](#) and is described below. The model also allows for external inputs ( $u$ ) which consists  
912 of extracted pose features including the distance between animals and the facing angle  
913 between the resident and intruder mouse.

914 The model is formulated as follows: At each time  $t = 1, 2, \dots, T_n$ , there is a discrete state  
915  $z_t \in \{1, 2, \dots, K\}$ . In a standard SLDS, these states follow Markovian dynamics, however  
916 rSLDS allows for the transitions between states to depend recurrently on the continuous  
917 latent factors ( $x$ ) and external inputs ( $u$ ) as follows:

$$p(z_{t+1} = k, z_t = j, x_t) \propto \exp\{Rx_t + Wu_t + r\} \quad (1)$$

918

919 where  $R$ ,  $W$  and  $r$  parameterizes a map from the previous discrete state, continuous state  
920 and external inputs using a softmax link function to a distribution over the next discrete  
921 states.

922 The discrete state  $z_t$  determines the linear dynamical system used to generate the  
923 continuous latent factors at any time  $t$ :

$$x_t = A_{z_t}x_{t-1} + V_{z_t}u_t + b_{z_t} \quad (2)$$

924 where  $A_k \in \mathbb{R}^{d \times d}$  is a dynamics matrix and  $b_k \in \mathbb{R}^d$  is a bias vector, where  $d$  is the  
925 dimensionality of the latent space. Thus, the discrete state specifies a set of linear

926 dynamical system parameters and specify which dynamics to use when updating the  
927 continuous latent factors.

928 Lastly, we can recover the activity of recorded neurons by modelling activity as a linear  
929 noisy Gaussian observation  $y_t \in \mathbb{R}^N$  where  $N$  is the number of recorded neurons:

$$y_t = Cx_t + d \quad (3)$$

930 For  $C \in \mathbb{R}^{N \times D}$  and  $d \sim N(0, S)$ , a gaussian random variable. Overall, the system  
931 parameters that rSLDS needs to learn consists of the state transition dynamics, library of  
932 linear dynamical system matrices and neuron-specific emission parameters, which we  
933 write as:

934

935

$$\theta = \{A_k, V_k, b_k, C, d, R, W, r\}$$

937 These parameters are estimated using maximum likelihood using approximate variational  
938 inference methods as described in detail in [Linderman et al., 2019](#).

939 Model performance is reported as the *evidence lower bound (ELBO)* which is equivalent  
940 to the Kullback-Leibler divergence between the approximate and true posterior,  
941  $KL(q(x, z; \varphi) || p(x, z | y; \theta))$  using 5-fold cross validation.

942 Code used to fit rSLDS on neural data is available in the SSM package:  
943 (<https://github.com/lindermanlab/ssm>)

#### 944 **Estimation of time constants**

945 We estimated the time constant of each mode of linear dynamical systems using  
946 eigenvalues  $\lambda_a$  of the dynamics matrix of that system, derived by [Maheswaranathan et](#)  
947 [al., 2019](#) as:

$$948 \quad \tau_a = \left| \frac{1}{\log(|\lambda_a|)} \right|$$

949

## 950 **Decoding behavior from integration dimension**

951 We trained a frame-wise decoder to discriminate pairs of behavior (such as sniffing vs  
952 attack) from the activity of the integration dimension on individual frames of a behavior  
953 (sampled at 15Hz) as described previously (Karigo et al., 2021). After merging bouts of  
954 behavior that were separated by less than 5 seconds, we trained a linear binary SVM,  
955 using 5-fold cross validation across intruder mice. Equal number of frames were used  
956 during decoder training to ensure chance decoder performance of 50%. ‘Shuffled’  
957 decoder data was generated by training the decoder on the same neural data but with  
958 behavior annotations randomly assigned to each behavior bout. Decoding was repeated  
959 20 times for each intruder and each mouse, and performance reported as the average  
960 accuracy across imaged mice.

## 961 **Dynamic velocity as a measure of stability in a dynamical system and visualization** 962 **as 3D landscape**

963 We devised a metric termed the “dynamic velocity” to quantify the average intrinsically  
964 generated rate of change of the fit dynamical system during a given behavior of interest.  
965 We first calculated the average norm of  $A_{z_t}x_t$  for every value of  $x_t$  associated with a given  
966 behavior, for a given state  $z$ . We then averaged this value across states, giving a definition  
967 of  $V_b = \frac{1}{n(Z)} \sum_{z \in Z} \left( \frac{1}{n(T_b)} \sum_{t \in T_b} \|A_{z_t}x_t\| \right)$ , where  $Z$  is the set of states,  $T_b$  is the set of all  
968 timepoints during which behavior  $b$  occurred,  $\|\cdot\|$  is the Euclidean norm, and  $n(\cdot)$  is the  
969 number of elements in a set. Finally, to facilitate comparison across animals, we  
970 normalized this value with respect to its maximum across behaviors in each animal.

971 We also converted the flow-fields obtained from rSLDS into a 3D landscape for  
972 visualization by calculating the dynamic velocity at each point in neural state space and  
973 using it as the height of a 3D landscape.

974

975

976

977 **Statistical analysis**

978 Data were processed and analyzed using Python, MATLAB, and GraphPad (GraphPad  
979 PRISM 9). All data were analyzed using two-tailed non-parametric tests. Mann-Whitney  
980 test were used for binary paired samples. Friedman test was used for non-binary paired  
981 samples. Kolmogorov-Smirnov test was used for non-paired samples. Multiple  
982 comparisons were corrected with Dunn's multiple comparisons correction. Not significant  
983 (NS),  $P > 0.05$ ; \* $P < 0.05$ ; \*\* $P < 0.01$ ; \*\*\* $P < 0.001$ ; \*\*\*\* $P < 0.0001$ .

984 **Works cited**

- 985 Anderson, D.J. (2016). Circuit modules linking internal states and social behaviour in flies and  
986 mice. *Nat Rev Neurosci* 17, 692-704.
- 987 Atasoy, D., Betley, J.N., Su, H.H., and Sternson, S.M. (2012). Deconstruction of a neural circuit  
988 for hunger. *Nature* 488, 172-177.
- 989 Augustine, V., Lee, S., and Oka, Y. (2020). Neural Control and Modulation of Thirst, Sodium  
990 Appetite, and Hunger. *Cell* 180, 25-32.
- 991 Canteras, N.S. (2002). The medial hypothalamic defensive system: hodological organization and  
992 functional implications. *Pharmacology Biochemistry and Behavior* 71, 481-491.
- 993 Chen, J., Markowitz, J.E., Lilascharoen, V., Taylor, S., Sheurpukdi, P., Keller, J.A., Jensen, J.R.,  
994 Lim, B.K., Datta, S.R., and Stowers, L. (2021). Flexible scaling and persistence of social vocal  
995 communication. *Nature* 593, 108-113.
- 996 Chen, P., and Hong, W. (2018). Neural Circuit Mechanisms of Social Behavior. *Neuron* 98, 16-  
997 30.
- 998 Covington, H.E., 3rd, Newman, E.L., Leonard, M.Z., and Miczek, K.A. (2019). Translational  
999 models of adaptive and excessive fighting: an emerging role for neural circuits in pathological  
1000 aggression. *F1000Res* 8.
- 1001 Ebitz, R.B., and Hayden, B.Y. (2021). The population doctrine in cognitive neuroscience. *Neuron*  
1002 109, 3055-3068.
- 1003 Evans, D.A., Stempel, A.V., Vale, R., Ruehle, S., Lefler, Y., and Branco, T. (2018). A synaptic  
1004 threshold mechanism for computing escape decisions. *Nature* 558, 590-594.
- 1005 Falkner, A.L., Dollar, P., Perona, P., Anderson, D.J., and Lin, D. (2014). Decoding ventromedial  
1006 hypothalamic neural activity during male mouse aggression. *J Neurosci* 34, 5971-5984.
- 1007 Falkner, A.L., Grosenick, L., Davidson, T.J., Deisseroth, K., and Lin, D. (2016). Hypothalamic  
1008 control of male aggression-seeking behavior. *Nature neuroscience* 19, 596-604.
- 1009 Falkner, A.L., Wei, D., Song, A., Watsek, L.W., Chen, I., Chen, P., Feng, J.E., and Lin, D. (2020).  
1010 Hierarchical representations of aggression in a hypothalamic-midbrain circuit. *Neuron* 106, 637-  
1011 648. e636.
- 1012 Fusi, S., Miller, E.K., and Rigotti, M. (2016). Why neurons mix: high dimensionality for higher  
1013 cognition. *Curr Opin Neurobiol* 37, 66-74.
- 1014 Ganguli, S., Bisley, J.W., Roitman, J.D., Shadlen, M.N., Goldberg, M.E., and Miller, K.D. (2008).  
1015 One-dimensional dynamics of attention and decision making in LIP. *Neuron* 58, 15-25.
- 1016 Gao, S.C., Wei, Y.C., Wang, S.R., and Xu, X.H. (2019). Medial Preoptic Area Modulates  
1017 Courtship Ultrasonic Vocalization in Adult Male Mice. *Neurosci Bull* 35, 697-708.

- 1018 Ghosh, K.K., Burns, L.D., Cocker, E.D., Nimmerjahn, A., Ziv, Y., El Gamal, A., and Schnitzer, M.J.  
1019 (2011). Miniaturized integration of a fluorescence microscope. *Nature methods* *8*, 871-878.
- 1020 Golden, S.A., Jin, M., and Shaham, Y. (2019). Animal Models of (or for) Aggression Reward,  
1021 Addiction, and Relapse: Behavior and Circuits. *J Neurosci* *39*, 3996-4008.
- 1022 Graybiel, A.M. (2000). The basal ganglia. *Curr Biol* *10*, R509-511.
- 1023 Hashikawa, K., Hashikawa, Y., Tremblay, R., Zhang, J., Feng, J.E., Sabol, A., Piper, W.T., Lee,  
1024 H., Rudy, B., and Lin, D. (2017a). *Esr1*+ cells in the ventromedial hypothalamus control female  
1025 aggression. *Nature neuroscience* *20*, 1580-1590.
- 1026 Hashikawa, Y., Hashikawa, K., Falkner, A.L., and Lin, D. (2017b). Ventromedial Hypothalamus  
1027 and the Generation of Aggression. *Front Syst Neurosci* *11*, 94.
- 1028 Hess, W.R. (1927). *Stammganglien-reizversuche* (Verlag Julius Springer).
- 1029 Hess, W.R., and Brügger, M. (1943). Das subkortikale Zentrum der affektiven Abwehrreaktion.  
1030 *Helvetica Physiologica et Pharmacologica Acta*.
- 1031 Hulse, B.K., and Jayaraman, V. (2020). Mechanisms underlying the neural computation of head  
1032 direction. *Annual review of neuroscience* *43*, 31-54.
- 1033 Inagaki, H.K., Fontolan, L., Romani, S., and Svoboda, K. (2019). Discrete attractor dynamics  
1034 underlies persistent activity in the frontal cortex. *Nature* *566*, 212-217.
- 1035 Ishii, K.K., Osakada, T., Mori, H., Miyasaka, N., Yoshihara, Y., Miyamichi, K., and Touhara, K.  
1036 (2017). A labeled-line neural circuit for pheromone-mediated sexual behaviors in mice. *Neuron*  
1037 *95*, 123-137. e128.
- 1038 Jazayeri, M., and Afraz, A. (2017). Navigating the Neural Space in Search of the Neural Code.  
1039 *Neuron* *93*, 1003-1014.
- 1040 Karigo, T., Kennedy, A., Yang, B., Liu, M., Tai, D., Wahle, I.A., and Anderson, D.J. (2021). Distinct  
1041 hypothalamic control of same-and opposite-sex mounting behaviour in mice. *Nature* *589*, 258-  
1042 263.
- 1043 Kennedy, A., Kunwar, P.S., Li, L.Y., Stagkourakis, S., Wagenaar, D.A., and Anderson, D.J. (2020).  
1044 Stimulus-specific hypothalamic encoding of a persistent defensive state. *Nature* *586*, 730-734.
- 1045 Kim, D.-W., Yao, Z., Graybuck, L.T., Kim, T.K., Nguyen, T.N., Smith, K.A., Fong, O., Yi, L.,  
1046 Kouloua, N., and Pierson, N. (2019). Multimodal analysis of cell types in a hypothalamic node  
1047 controlling social behavior. *Cell* *179*, 713-728. e717.
- 1048 Klaus, A., Alves da Silva, J., and Costa, R.M. (2019). What, If, and When to Move: Basal Ganglia  
1049 Circuits and Self-Paced Action Initiation. *Annu Rev Neurosci* *42*, 459-483.
- 1050 Kohl, J., Babayan, B.M., Rubinstein, N.D., Autry, A.E., Marin-Rodriguez, B., Kapoor, V., Miyamishi,  
1051 K., Zweifel, L.S., Luo, L., and Uchida, N. (2018). Functional circuit architecture underlying parental  
1052 behaviour. *Nature* *556*, 326-331.

- 1053 Lee, H., Kim, D.W., Remedios, R., Anthony, T.E., Chang, A., Madisen, L., Zeng, H., and Anderson,  
1054 D.J. (2014). Scalable control of mounting and attack by *Esr1*<sup>+</sup> neurons in the ventromedial  
1055 hypothalamus. *Nature* 509, 627-632.
- 1056 Leibowitz, S.F. (1992). Neurochemical-neuroendocrine systems in the brain controlling  
1057 macronutrient intake and metabolism. *Trends in neurosciences* 15, 491-497.
- 1058 Lin, D., Boyle, M.P., Dollar, P., Lee, H., Lein, E.S., Perona, P., and Anderson, D.J. (2011).  
1059 Functional identification of an aggression locus in the mouse hypothalamus. *Nature* 470, 221-226.
- 1060 Linderman, S., Johnson, M., Miller, A., Adams, R., Blei, D., and Paninski, L. (2017). Bayesian  
1061 learning and inference in recurrent switching linear dynamical systems. Paper presented at:  
1062 Artificial Intelligence and Statistics (PMLR).
- 1063 Linderman, S., Nichols, A., Blei, D., Zimmer, M., and Paninski, L. (2019). Hierarchical recurrent  
1064 state space models reveal discrete and continuous dynamics of neural activity in *C. elegans*.  
1065 BioRxiv, 621540.
- 1066 Liu, M., Kim, D.W., Zeng, H., and Anderson, D.J. (2022). Make war not love: The neural substrate  
1067 underlying a state-dependent switch in female social behavior. *Neuron*.
- 1068 Lo, L., Yao, S., Kim, D.W., Cetin, A., Harris, J., Zeng, H., Anderson, D.J., and Weissbourd, B.  
1069 (2019). Connectional architecture of a mouse hypothalamic circuit node controlling social  
1070 behavior. *Proc Natl Acad Sci U S A* 116, 7503-7512.
- 1071 Maheswaranathan, N., Williams, A.H., Golub, M.D., Ganguli, S., and Sussillo, D. (2019). Reverse  
1072 engineering recurrent networks for sentiment classification reveals line attractor dynamics.  
1073 *Advances in neural information processing systems* 32, 15696.
- 1074 Mante, V., Sussillo, D., Shenoy, K.V., and Newsome, W.T. (2013). Context-dependent  
1075 computation by recurrent dynamics in prefrontal cortex. *nature* 503, 78-84.
- 1076 McKellar, C.E., Lillvis, J.L., Bath, D.E., Fitzgerald, J.E., Cannon, J.G., Simpson, J.H., and Dickson,  
1077 B.J. (2019). Threshold-Based Ordering of Sequential Actions during *Drosophila* Courtship. *Curr*  
1078 *Biol* 29, 426-434 e426.
- 1079 Moffitt, J.R., Bambah-Mukku, D., Eichhorn, S.W., Vaughn, E., Shekhar, K., Perez, J.D.,  
1080 Rubinstein, N.D., Hao, J., Regev, A., and Dulac, C. (2018). Molecular, spatial, and functional  
1081 single-cell profiling of the hypothalamic preoptic region. *Science* 362.
- 1082 Nelson, R.J., and Trainor, B.C. (2007). Neural mechanisms of aggression. *Nat Rev Neurosci* 8,  
1083 536-546.
- 1084 Park, J., Coddington, L.T., and Dudman, J.T. (2020). Basal Ganglia Circuits for Action  
1085 Specification. *Annu Rev Neurosci* 43, 485-507.
- 1086 Remedios, R., Kennedy, A., Zelikowsky, M., Grewe, B.F., Schnitzer, M.J., and Anderson, D.J.  
1087 (2017). Social behaviour shapes hypothalamic neural ensemble representations of conspecific  
1088 sex. *Nature* 550, 388-392.

- 1089 Sabatini, B.L., and Tian, L. (2020). Imaging Neurotransmitter and Neuromodulator Dynamics In  
1090 Vivo with Genetically Encoded Indicators. *Neuron* 108, 17-32.
- 1091 Saper, C.B., and Lowell, B.B. (2014). The hypothalamus. *Curr Biol* 24, R1111-1116.
- 1092 Segalin, C., Williams, J., Karigo, T., Hui, M., Zelikowsky, M., Sun, J.J., Perona, P., Anderson, D.J.,  
1093 and Kennedy, A. (2021). The Mouse Action Recognition System (MARS) software pipeline for  
1094 automated analysis of social behaviors in mice. *Elife* 10.
- 1095 Seung, H.S. (1996). How the brain keeps the eyes still. *Proceedings of the National Academy of*  
1096 *Sciences* 93, 13339-13344.
- 1097 Shenoy, K.V., Sahani, M., and Churchland, M.M. (2013). Cortical control of arm movements: a  
1098 dynamical systems perspective. *Annual review of neuroscience* 36, 337-359.
- 1099 Stagkourakis, S., Spigolon, G., Liu, G., and Anderson, D.J. (2020). Experience-dependent  
1100 plasticity in an innate social behavior is mediated by hypothalamic LTP. *Proc Natl Acad Sci U S*  
1101 *A* 117, 25789-25799.
- 1102 Stagkourakis, S., Spigolon, G., Williams, P., Protzmann, J., Fisone, G., and Broberger, C. (2018).  
1103 A neural network for intermale aggression to establish social hierarchy. *Nat Neurosci* 21, 834-842.
- 1104 Sternson, S.M. (2013). Hypothalamic survival circuits: blueprints for purposive behaviors. *Neuron*  
1105 77, 810-824.
- 1106 Strogatz, S.H. (2018). *Nonlinear dynamics and chaos with student solutions manual: With*  
1107 *applications to physics, biology, chemistry, and engineering* (CRC press).
- 1108 Sun, F., Zeng, J., Jing, M., Zhou, J., Feng, J., Owen, S.F., Luo, Y., Li, F., Wang, H., Yamaguchi,  
1109 T., *et al.* (2018). A Genetically Encoded Fluorescent Sensor Enables Rapid and Specific Detection  
1110 of Dopamine in Flies, Fish, and Mice. *Cell* 174, 481-496 e419.
- 1111 Tinbergen, N. (1951). *The study of instinct* (Oxford).
- 1112 Tschida, K., Michael, V., Takato, J., Han, B.X., Zhao, S., Sakurai, K., Mooney, R., and Wang, F.  
1113 (2019). A Specialized Neural Circuit Gates Social Vocalizations in the Mouse. *Neuron* 103, 459-  
1114 472 e454.
- 1115 Vyas, S., Golub, M.D., Sussillo, D., and Shenoy, K.V. (2020). Computation through neural  
1116 population dynamics. *Annual Review of Neuroscience* 43, 249-275.
- 1117 Wei, Y.-C., Wang, S.-R., Jiao, Z.-L., Zhang, W., Lin, J.-K., Li, X.-Y., Li, S.-S., Zhang, X., and Xu,  
1118 X.-H. (2018). Medial preoptic area in mice is capable of mediating sexually dimorphic behaviors  
1119 regardless of gender. *Nature communications* 9, 1-15.
- 1120 Wu, Z., Autry, A.E., Bergan, J.F., Watabe-Uchida, M., and Dulac, C.G. (2014). Galanin neurons  
1121 in the medial preoptic area govern parental behaviour. *Nature* 509, 325-330.
- 1122 Xie, Z., Gu, H., Huang, M., Cheng, X., Shang, C., Tao, T., Li, D., Xie, Y., Zhao, J., Lu, W., *et al.*  
1123 (2022). Mechanically evoked defensive attack is controlled by GABAergic neurons in the anterior  
1124 hypothalamic nucleus. *Nat Neurosci* 25, 72-85.

- 1125 Yang, B., and Anderson, D.J. (2022). Transformations and functions of neural representations in  
1126 a subcortical behavior network. Under Review.
- 1127 Yang, C.F., Chiang, M.C., Gray, D.C., Prabhakaran, M., Alvarado, M., Juntti, S.A., Unger, E.K.,  
1128 Wells, J.A., and Shah, N.M. (2013). Sexually dimorphic neurons in the ventromedial  
1129 hypothalamus govern mating in both sexes and aggression in males. *Cell* 153, 896-909.
- 1130 Yang, C.F., and Shah, N.M. (2014). Representing sex in the brain, one module at a time. *Neuron*  
1131 82, 261-278.
- 1132 Yang, T., Yang, C.F., Chizari, M.D., Maheswaranathan, N., Burke, K.J., Jr., Borius, M., Inoue, S.,  
1133 Chiang, M.C., Bender, K.J., Ganguli, S., *et al.* (2017). Social Control of Hypothalamus-Mediated  
1134 Male Aggression. *Neuron* 95, 955-970 e954.
- 1135 Zha, X., and Xu, X.H. (2021). Neural circuit mechanisms that govern inter-male attack in mice.  
1136 *Cell Mol Life Sci* 78, 7289-7307.
- 1137 Zhang, S.X., Lutas, A., Yang, S., Diaz, A., Fluhr, H., Nagel, G., Gao, S., and Andermann, M.L.  
1138 (2021). Hypothalamic dopamine neurons motivate mating through persistent cAMP signalling.  
1139 *Nature* 597, 245-249.
- 1140 Zhu, Z., Ma, Q., Yang, H., Miao, L., Pan, L., Li, K., Zhang, X., Wu, J., Hao, S., and Lin, S. (2020).  
1141 A Substantia Innominata-midbrain Circuit Controls a General Aggressive State. *bioRxiv*.
- 1142 Ziv, Y., Burns, L.D., Cocker, E.D., Hamel, E.O., Ghosh, K.K., Kitch, L.J., El Gamal, A., and  
1143 Schnitzer, M.J. (2013). Long-term dynamics of CA1 hippocampal place codes. *Nature*  
1144 *neuroscience* 16, 264-266.
- 1145

# Figure 1

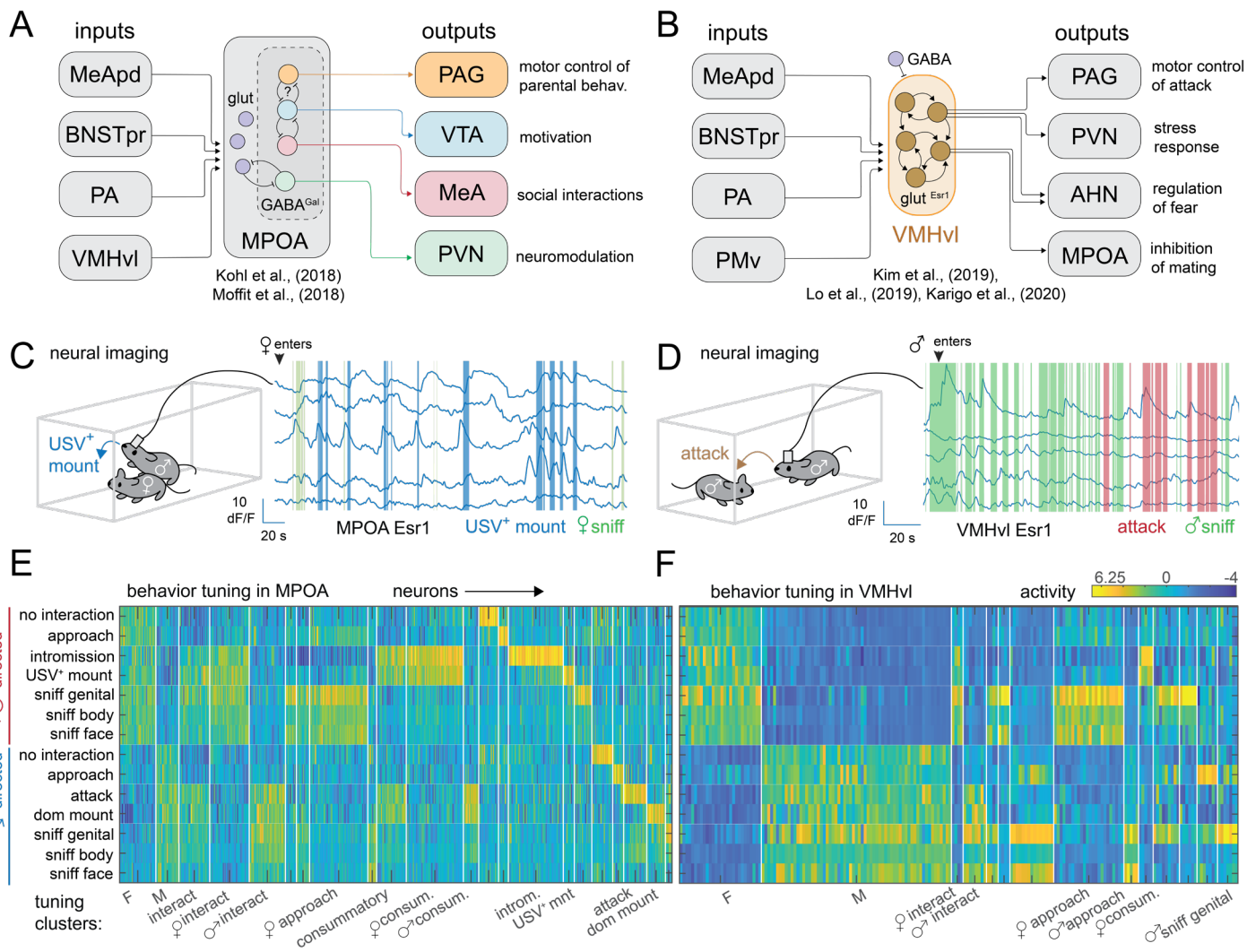


## Figure 2

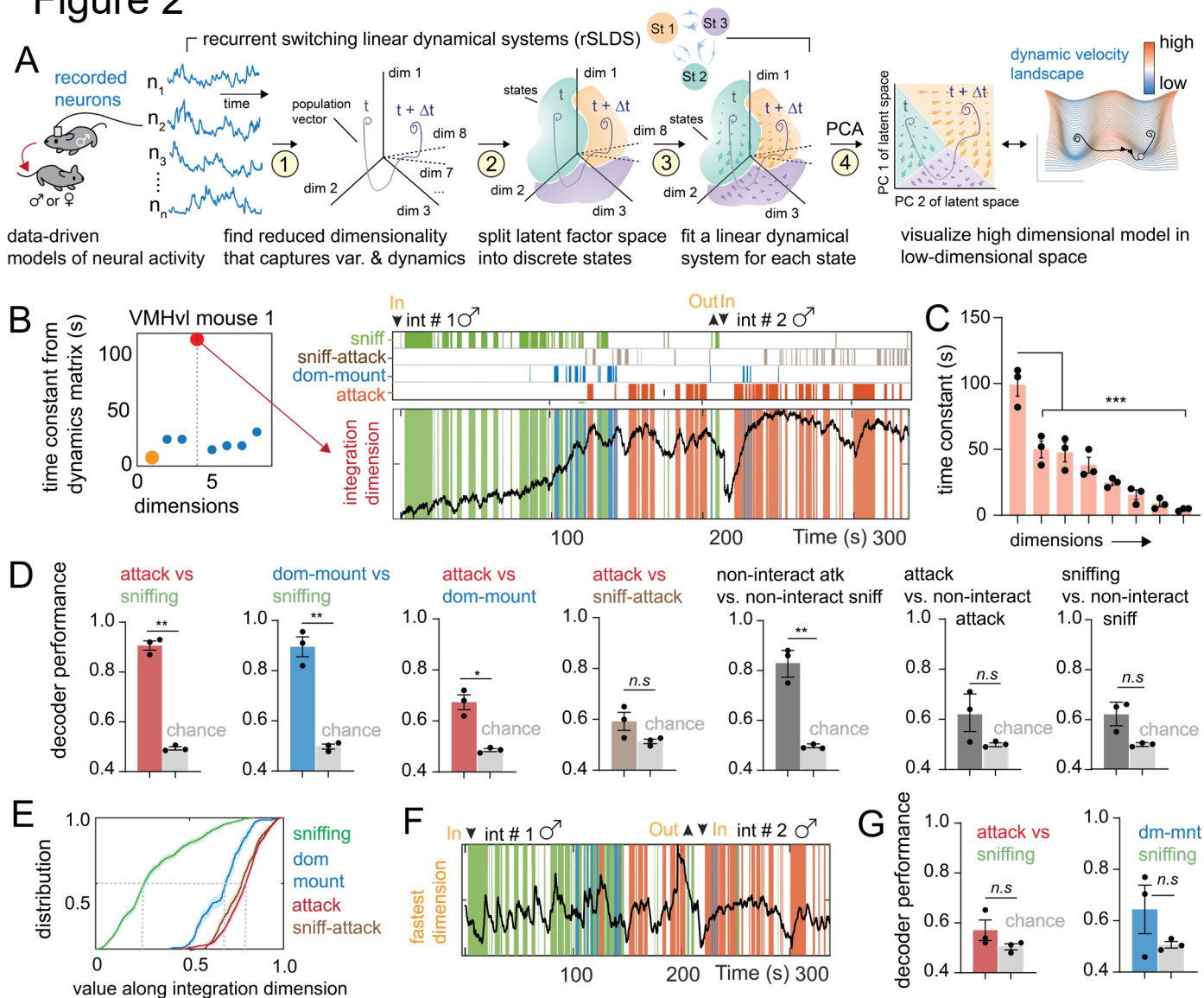


# Figure 3

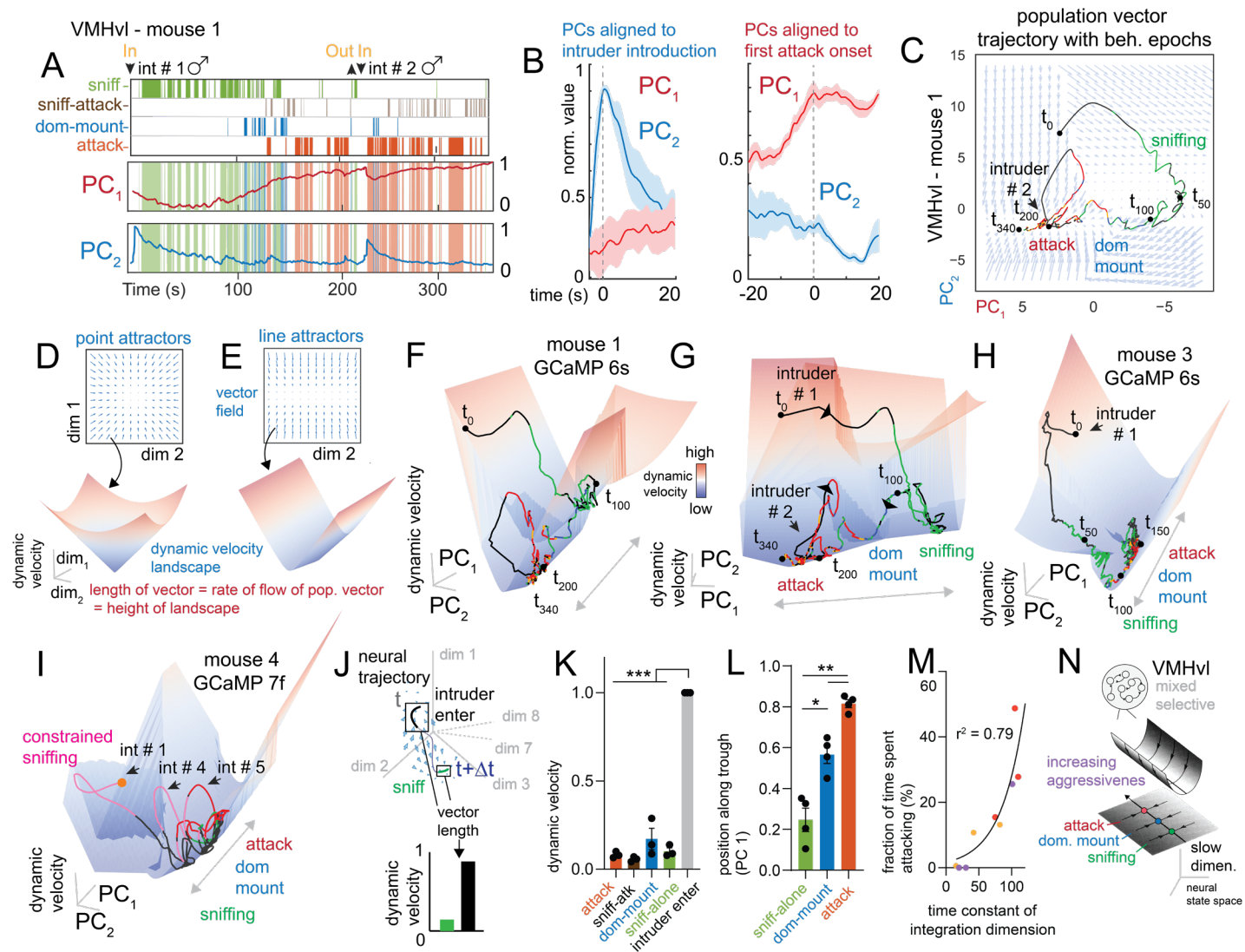


# Figure 4

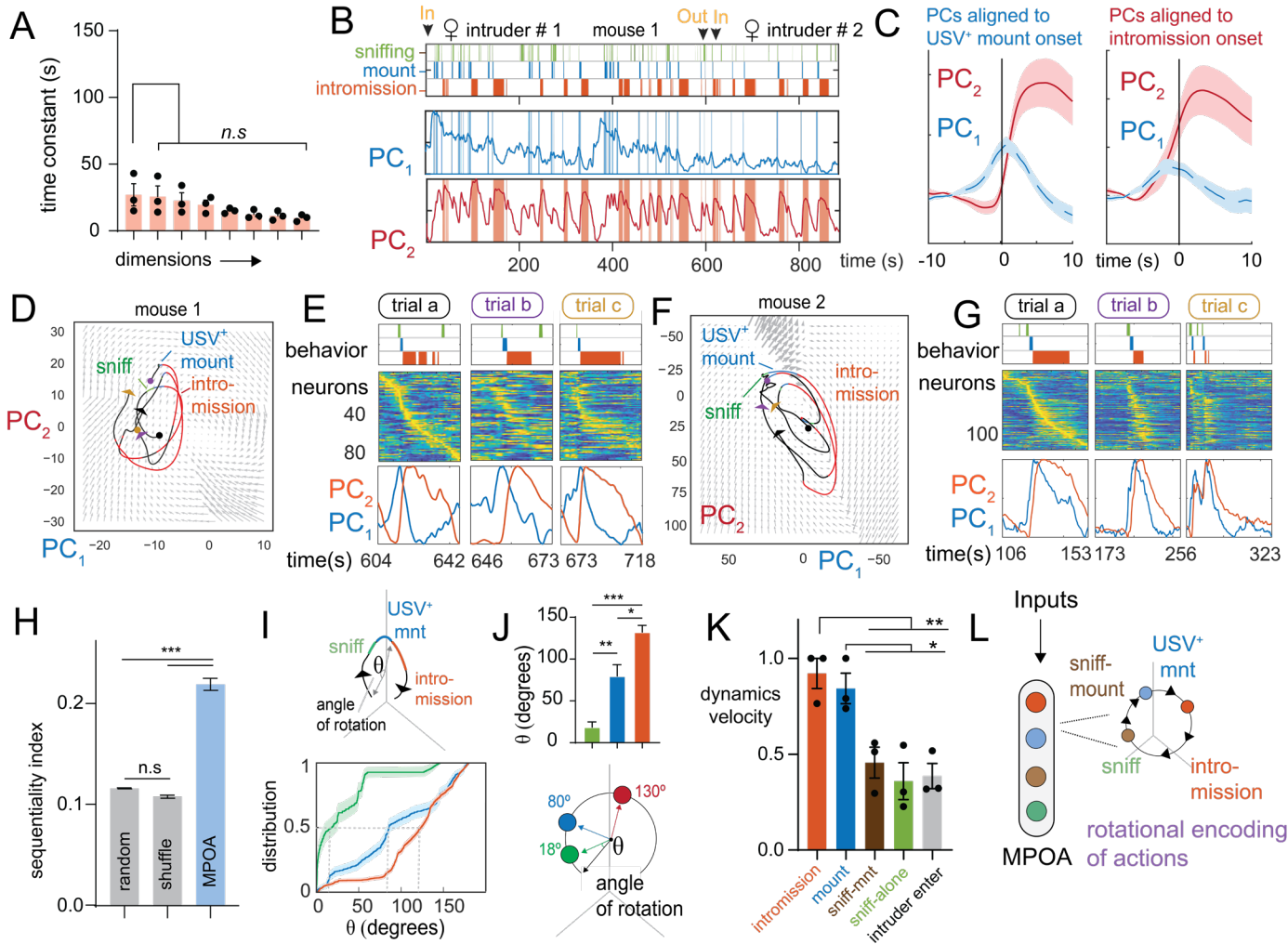


# Figure 5

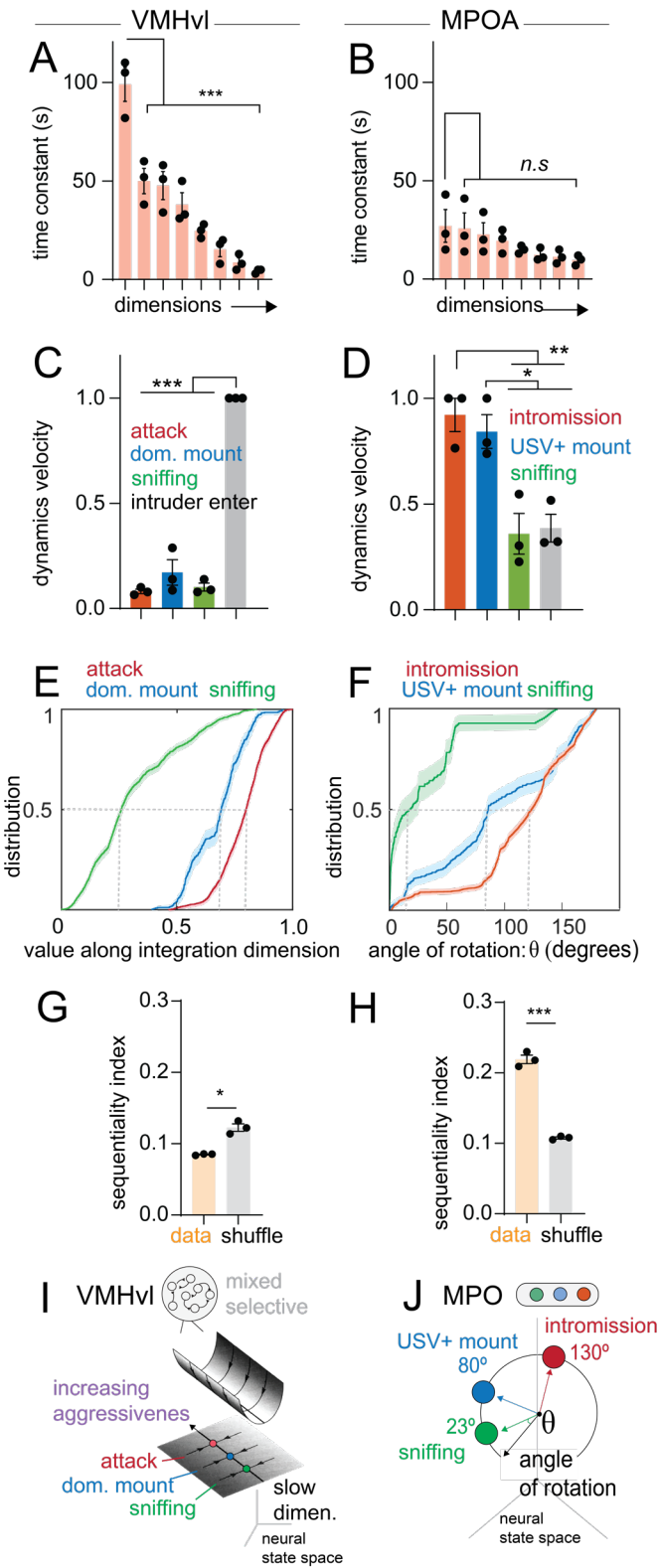
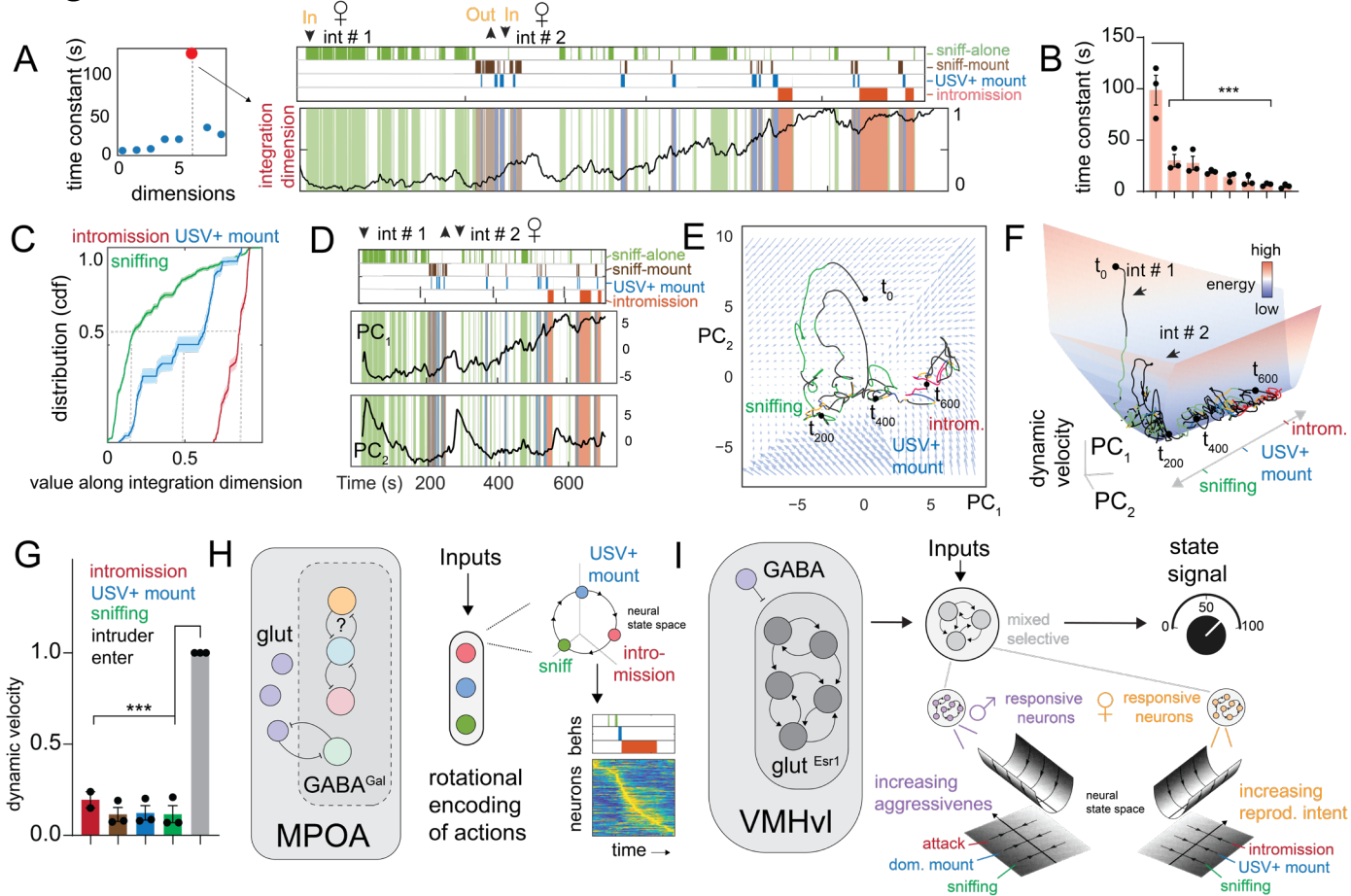
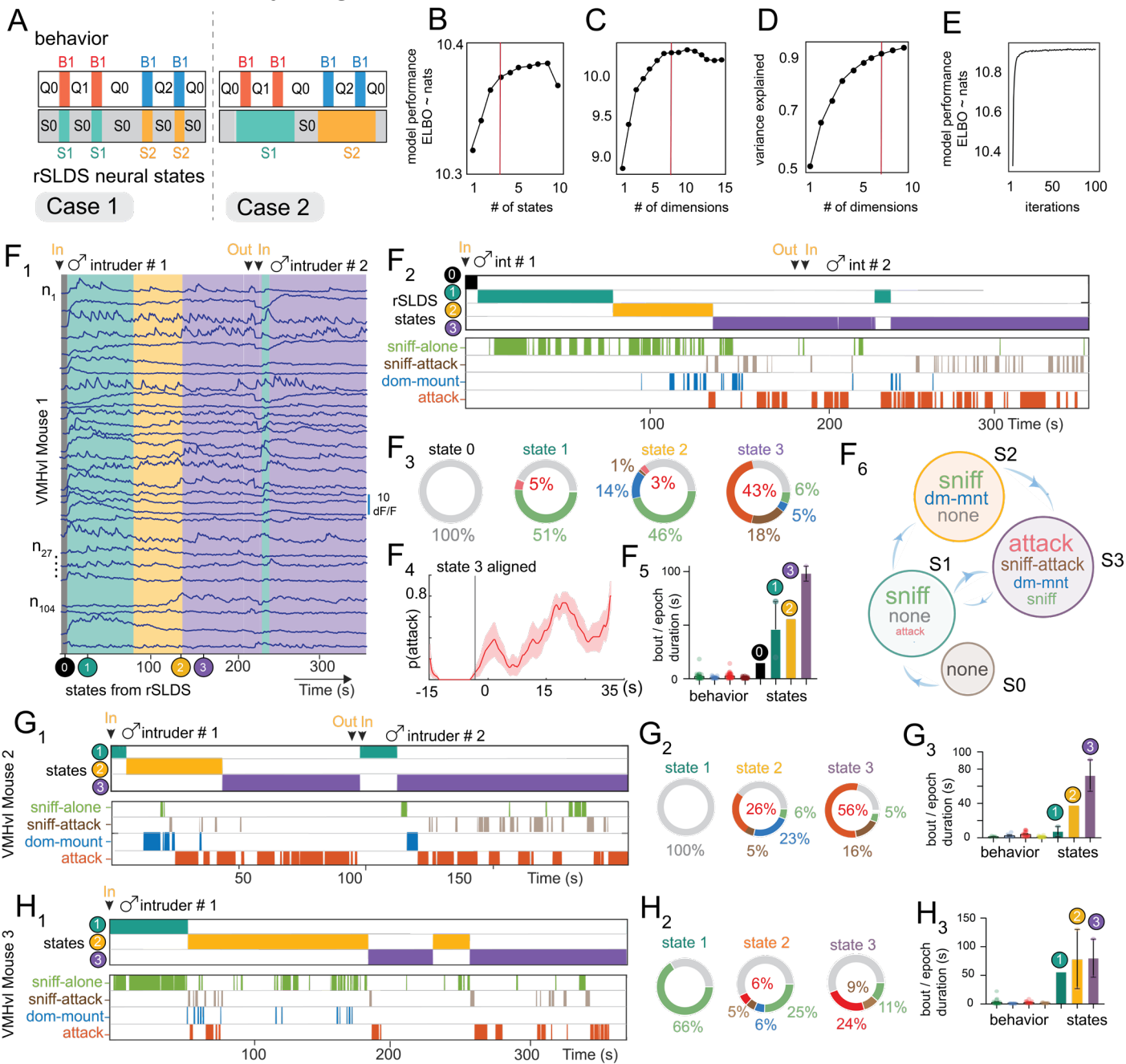


# Figure 6



# Supplementary Figure 1

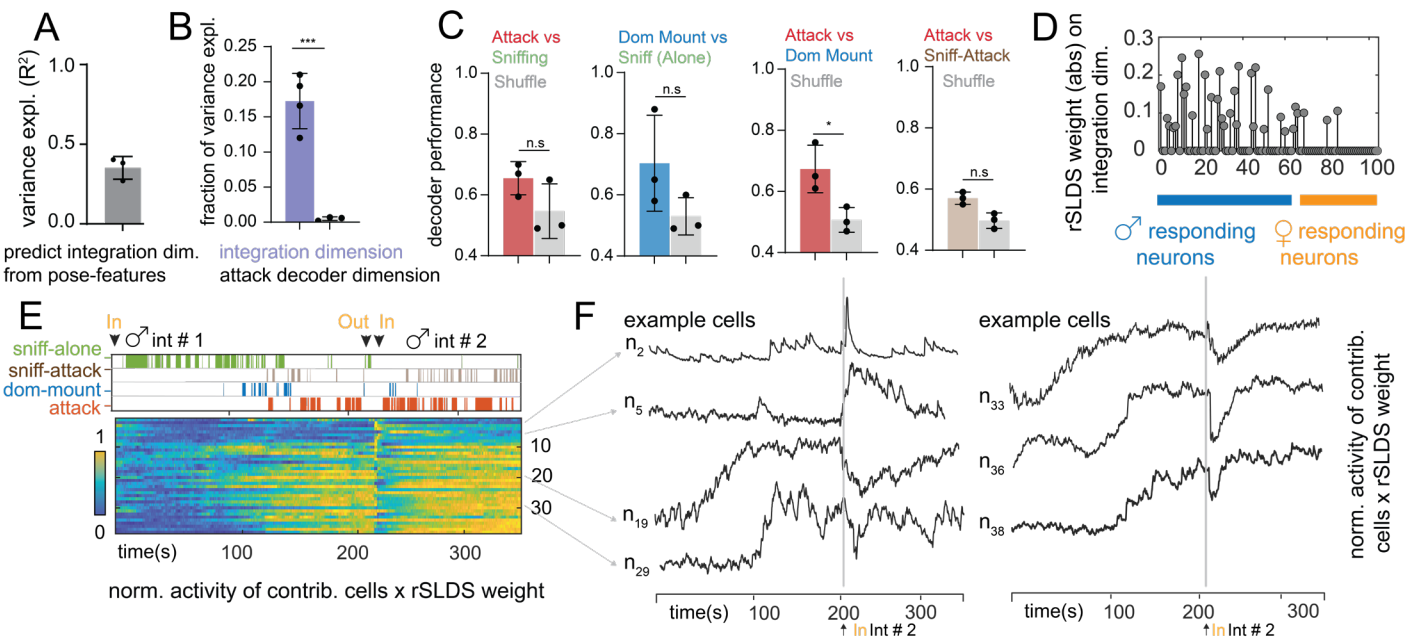


## Supplementary Figure 1: Unsupervised discovery of aggression-enriched states in VMHvl

Related to Figure 2

**A:** types of neural states that may be identified by rSLDS. B1, B2: behaviors; Q0, Q1: periods of quiescence between behavior bouts; S0,S1: rSLDS states discovered by analysis of neural data. Case 1 is when rSLDS states cannot distinguish behavior vs internal states. Case 2 is when rSLDS reflects internal state-encoding due to persistence during behavioral quiescence. **B:** optimization of number of states for rSLDS in example VMHvl mouse. Model performance is measured as the evidence of lower bound of the log-likelihood (ELBO). **C:** same as B, but for dimensionality. **D:** variance explained by dimension chosen in C. **E:** convergence of model performance. **F<sub>1</sub>:** rSLDS segments neural activity into various long-lived states in VMHvl mouse 1. **F<sub>2</sub>:** comparison of discovered states with behaviors performed by VMHvl mouse 1. **F<sub>3</sub>:** behavioral composition of discovered states highlights states with various amount of aggressive behavior. State 3 possesses the highest amount of attack behavior across mice (see panel I, N). **F<sub>4</sub>:** probability of attack aligned to the onset of state 3 across animals (n = 3 mice). **F<sub>5</sub>:** timescale of behavior bouts compared to the that of discovered states epochs. **F<sub>6</sub>:** state transition diagram from empirical transition probabilities. **G:** Same as F<sub>2</sub>, F<sub>3</sub>, F<sub>5</sub> but for VMHvl mouse 2. **H:** Same as F<sub>2</sub>, F<sub>3</sub>, F<sub>5</sub> but for VMHvl mouse 3.

# Supplementary Figure 2

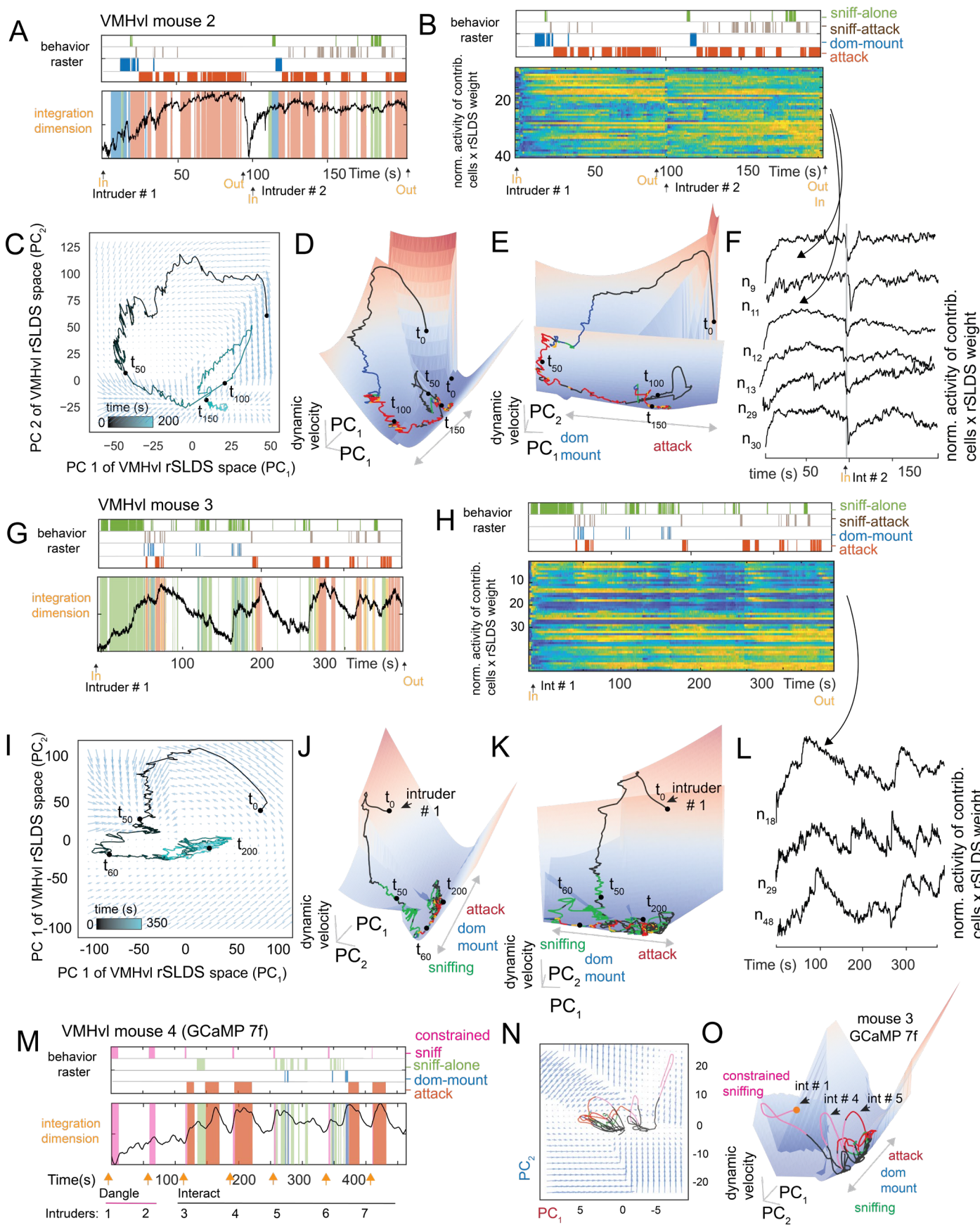


## Supplementary Figure 2: Characterization of aggression-integration dimension

Related to Figure 2

**A:** variance explained by GLM trained to predict integration dimension from pose-features including distance between mice, facing angle, speed, acceleration and velocity of resident mouse (mean:  $0.35 \pm 0.04 R^2$ ,  $n = 3$  mice). **B:** fraction of overall variance explained by integration dimension (purple) compared to variance explained by decoder dimension trained to distinguish attack from sniff bouts (integration dimension mean:  $0.17 \pm 0.02$ , attack decoder mean:  $0.005 \pm 0.001$ ,  $n = 4$  mice,  $***p < 0.001$ ). **C:** decoding behaviors from non-integration dimensions (average across dimensions,  $n = 3$  mice). **D:** absolute rSLDS weight on integration dimension of VMHvl mouse 1, sorted by choice probability values for male vs female intruder encounter. **E:** normalized activity of neurons times rSLDS weight for cells with significant weights for integration dimension of VMHvl mouse 1. **F:** example cells from D.

# Supplementary Figure 3

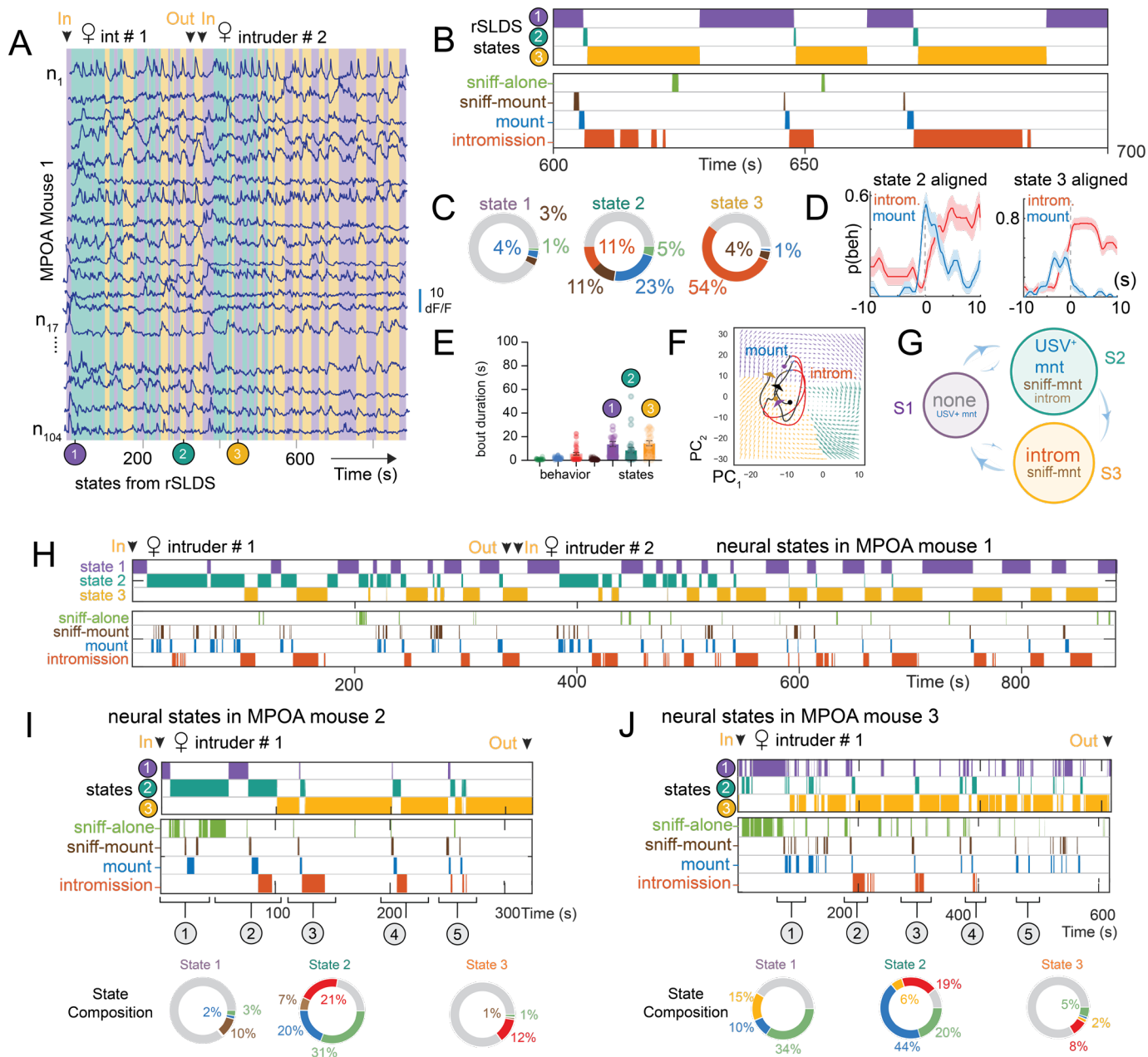


### **Supplementary Figure 3: Discovery of approximate line attractor dynamics in VMHvl (mouse 2, 3 and 4)**

Related to Figure 3

**A:** integration dimension of VMHvl mouse 2. **B:** normalized activity times rSLDS weight for cells contributing significantly to integration dimension of VMHvl mouse 2. **C:** neural state space of VMHvl mouse 2 with population trajectory overlaid over inferred flow field. **D, E:** dynamic velocity landscape of VMHvl mouse 2 showing trough shaped landscape. **F:** example cell activity from B. **G-L:** Same as A-F but for VMHvl mouse 3. **M:** integration dimension of VMHvl mouse 4. **N:** neural state space of VMHvl mouse 2 with population trajectory overlaid over inferred flow field. **O:** dynamic velocity landscape of VMHvl mouse 4 showing trough shaped landscape.

# Supplementary Figure 4



## Supplementary Figure 4: Unsupervised discovery of states by rSLDS in MPOA

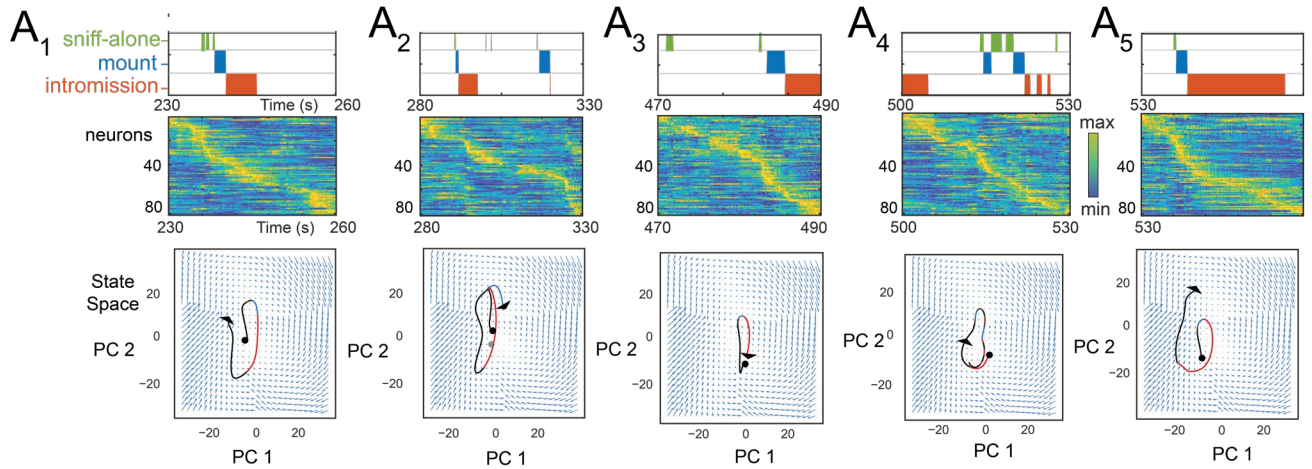
Related to Figure 4

**A:** rSLDS segments neural activity into several short-lived states in MPOA mouse 1. **B:** states identified by rSLDS are closely aligned to behaviors performed by the resident mouse. **C:** behavioral composition of discovered states. **D:** probability of intromission and USV+ mounting aligned to the onset of state 2 and state 3 across animals (also see panel I, J, n = 3 mice). **E:** timescale of behavioral bouts and bouts of states. **F:** Same as Figure 4D but with state-specific inferred flow-field colors. **G:** state transition diagram from empirically calculated transition probabilities. **H:** state and behavior raster for MPOA mouse 1. **I:** state and behavior raster for MPOA mouse 2 (top). Behavioral composition of discovered states (bottom). **J:** same as I for MPOA mouse 3.

# Supplementary Figure 5

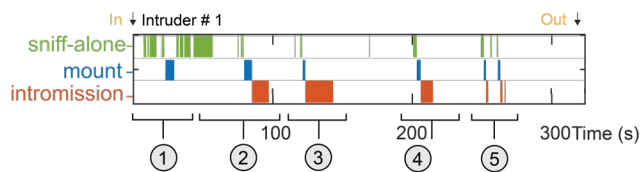
rotational dynamics in MPOA mouse 1

behaviour key sniff-alone sniff-mount unannotated USV<sup>+</sup> mount intromission



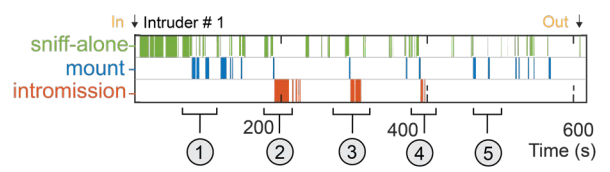
**B**

MPOA mouse 2



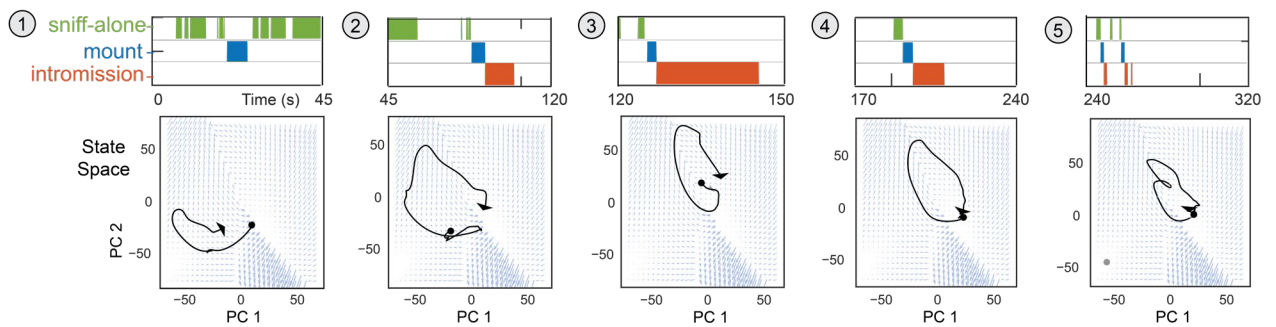
**C**

MPOA mouse 3



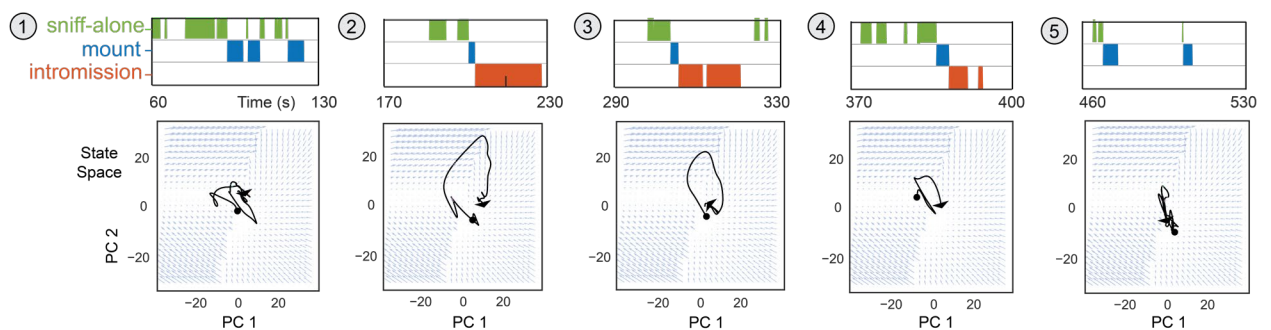
**D**

rotational dynamics in MPOA mouse 2



**E**

rotational dynamics in MPOA mouse 3

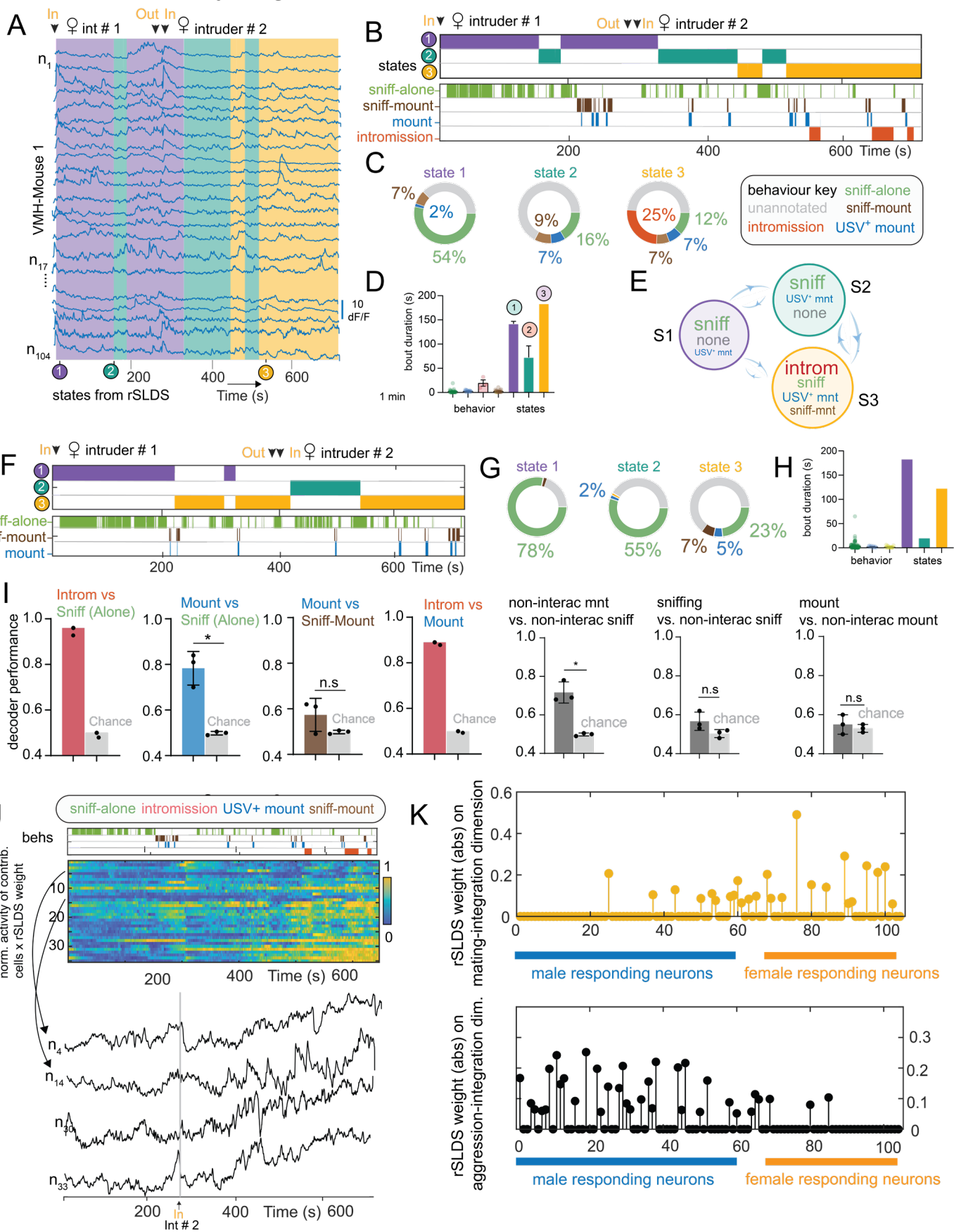


## Supplementary Figure 5: Rotational dynamics with sequential activity in MPOA

Related to Figure 4

**A<sub>1</sub>-A<sub>5</sub>**: Individual rotational trajectories for 5 mating episodes in MPOA mouse 1. **B,D**: Individual rotational trajectories for mating episodes in MPOA mouse 2. **C,E**: Rotational trajectories for mating episodes in MPOA mouse 3.

# Supplementary Figure 6



## Supplementary Figure 6: Unsupervised discover of mating-enriched states in VMHvl and characterization of mating-integration dimension

Related to Figure 6

**A:** rSLDS segments neural activity into various long-lived mating states in VMHvl mouse 1 during interactions with female intruders. **B:** comparison of discovered states with behaviors performed by VMHvl mouse 1. **C:** behavioral composition of discovered states highlights states with various amount of mating behavior. State 3 possesses the highest amount of mating behavior across mice (see panel H). **D:** timescale of behavior bouts compared to the that of discovered states epochs. **E:** state transition diagram from empirical transition probabilities. **F-H:** Same as B-D for VMHvl mouse 2. **I:** decoding behaviors from integration dimension (\* $p < 0.01$ ,  $n = 2$  mice for intromission vs sniffing and intromission vs mounting,  $n = 3$  mice for all other comparisons). **J:** normalized activity times rSLDS weight for cells contributing significantly to integration dimension of VMHvl mouse 1. **K:** absolute rSLDS weight on integration dimension of VMHvl mouse 1 during mating behavior (top, yellow dots) and aggression (bottom, black dots) sorted by choice probability values for male vs female intruder encounter.